JGR Atmospheres

RESEARCH ARTICLE
10.1029/2019JD030967

Key Points:
- Aerosol absorption is sensitive to mixing state, brown carbon, and soil dust optical properties
- Blanching reduces coating brown carbon radiative effect; soil dust radiative effect uncertainty due to the refractive index is large
- Radiative effect of radiation-absorbing aerosol total uncertainty is mainly due to dust refractive index and brown carbon treatment

Supporting Information:
- Supporting Information S1

Correspondence to:
P. Tuccella,
paolo.tuccella@aquila.infn.it;
paolo.tuccella@univaq.it

Citation:
Tuccella, P., Curci, G., Pitari, G., Lee, S., & Jo, D. S. (2020). Direct radiative effect of absorbing aerosols: Sensitivity to mixing state, brown carbon, and soil dust refractive index and shape. *Journal of Geophysical Research: Atmospheres*, *125*, e2019JD030967. https://doi.org/10.1029/2019JD030967

Received 8 MAY 2019
Accepted 3 JAN 2020
Accepted article online 8 JAN 2020

Author Contributions:
Conceptualization: Paolo Tuccella, Gabriele Curci, Giovanni Pitari
Formal analysis: Paolo Tuccella
Funding acquisition: Paolo Tuccella, Gabriele Curci, Giovanni Pitari
Investigation: Paolo Tuccella
Methodology: Paolo Tuccella
Project administration: Paolo Tuccella
Software: Paolo Tuccella, Gabriele Curci, Seungun Lee, Duseong S. Jo
Validation: Paolo Tuccella
Writing - original draft: Paolo Tuccella
Writing – review & editing: Paolo Tuccella, Gabriele Curci, Giovanni Pitari, Seungun Lee, Duseong S. Jo

Direct Radiative Effect of Absorbing Aerosols: Sensitivity to Mixing State, Brown Carbon, and Soil Dust Refractive Index and Shape

Paolo Tuccella[1,2], Gabriele Curci[1,2], Giovanni Pitari[1], Seungun Lee[3], and Duseong S. Jo[4,5]

[1]Department of Physical and Chemical Sciences, University of L'Aquila, L'Aquila, Italy, [2]Center of Excellence in Telesensing of Environment and Model Prediction of Severe Events, University of L'Aquila, L'Aquila, Italy, [3]School of Earth and Environmental Sciences, Seoul National University, Seoul, South Korea, [4]Cooperative Institute for Research in Environmental Sciences, University of Colorado Boulder, Boulder, CO, USA, [5]Department of Chemistry, University of Colorado Boulder, Boulder, CO, USA

Abstract Black carbon (BC), brown carbon (BrC), and soil dust are the most relevant radiation-absorbing aerosols in the climate system, and uncertainties of their absorbing optical properties are large. We performed a 5-year simulation with the GEOS-Chem global chemistry and transport model and calculated the aerosol optical properties testing different mixing state assumptions and absorption properties of BC and BrC, refractive index, and shape of soil dust. We found that the core-shell (CS) internal mixing representation produces the most accurate absorption aerosol optical depth and single-scattering albedo at Aerosol Robotic Network (AERONET) Sun photometers site observations dominated by carbonaceous absorption. Dust absorption is sensitive to the assumed refractive index. The nonspherical shape of dust improves the simulation at sites dominated by dust absorption. Global mean of all-sky direct radiative effect (DRE) by BC is +0.13 and +0.25 W/m^2 for external and CS mixing state assumptions, respectively. Adding BrC in CS mixing state, the BC-BrC DRE mixture increases to +0.40 W/m^2, indicating an absorption enhancement with respect to external mixing state of +0.27 W/m^2, which is less than the +0.51 W/m^2 previously reported. The difference is attributed to the inclusion of the blanching process of BrC from biomass burning. Dust DREs are −0.10, +0.11, and +0.22 W/m^2 for "low," "middle," and "high" dust absorption scenarios, respectively. Considering the nonspherical shape, these values change by up to 0.03 W/m^2. All-sky DRE by all radiation-absorbing aerosols is +0.46 W/m^2. Aerosol mixing state, BrC treatment, and dust optical property uncertainties suggest a total DRE uncertainty of −57%/+59%.

1. Introduction

In the last decades, the scientific community has recognized that the observed climate change is determined by both long-lived greenhouse gases and short-lived climate forcers, such as aerosol particles (Boucher et al., 2013). Atmospheric aerosols directly alter the budget of the surface radiation by scattering and absorbing both solar and terrestrial radiation (Haywood & Boucher, 2000), and they indirectly affect cloud properties and precipitation patterns because they act as cloud condensation nuclei (CCN) and ice nuclei (IN) (Andreae & Rosenfeld, 2008). In addition, some aerosol species, such as mineral dust, black carbon (BC), and brown carbon (BrC), heat the atmosphere while absorbing solar radiation. The resulting warming may locally enhance the atmospheric stability, leading to a decrease in cloud cover through the so-called semidirect effect (Hansen et al., 1997). The global mean radiative forcing (RF) due to aerosols, as a result of changes in anthropogenic emissions since preindustrial times, is highly uncertain and is estimated to be −0.9 W/m^2, with an uncertainty range from −1.9 to −0.1 W/m^2 (Boucher et al., 2013).

BC is emitted by diesel engines, industry, residential solid fuel, and biomass burning (BB; Bond et al., 2013). BC is very efficient in absorbing the incoming solar radiation, and it may affect the climate by acting as CCN for liquid water cloud and IN for mixed-phase and cirrus clouds (Boucher et al., 2013). Current estimates suggest that BC is the second most important climate forcing species after carbon dioxide (Gustafsson & Ramanathan, 2016). The climatic impact from black carbon emissions (as well as any aerosol particle species) is evaluated through the direct radiative effect (DRE) and direct radiative forcing (DRF). DRE is the instantaneous radiative impact; DRF is the change in DRE from preindustrial times to the present day

(Heald et al., 2014). Current estimates of anthropogenic BC DRF from fossil fuel (FF) and biofuel (BF) sources differ by more than a factor of 2 (Boucher et al., 2013). For example, Bond et al. (2013) reported a value of +0.71 W/m^2 with 90% uncertainty bounds of +0.08/+1.27 W/m^2. Recently, Wang et al. (2014), revising the ageing mechanism and optical properties of BC, including the absorption enhancement of BC coated with a nonabsorbing shell and the absorption from BrC, have reported a DRF of +0.21 W/m^2, lower than previous estimates.

BrC is considered the absorbing fraction of organic aerosol (OA; Andreae & Gelencsér, 2006; Laskin et al., 2015). Most climate models consider OA as scattering only, but some studies showed that OA may absorb the visible radiation, especially for wavelengths less than 400 nm (Lukács et al., 2007; Alexander et al., 2008; Chen & Bond, 2010; Arola et al., 2011; Kirchstetter & Thatcher, 2012). As a result, according to Jo et al. (2016), BrC reduces the cooling effect of OA by approximately 16%. The chemical composition of BrC is not completely understood. Observations indicate that BB, BF combustion, and ageing of secondary organic aerosol (SOA) are important BrC sources (Hecobian et al., 2010; Bones et al., 2010; Arola et al., 2011; Updyke et al., 2012; Lambe et al., 2013; Laskin et al., 2015; Yan et al., 2017). Another source of BrC is in-cloud heterogeneous processing (Y. Zhang et al., 2017). Hecobian et al. (2010) suggest that BB and SOA ageing represent 55% and 26–34% of BrC sources, respectively.

Currently, the treatment of BrC in atmospheric models is limited by the lack of mass and absorption observations. Few modeling studies have attempted to simulate BrC (Park et al., 2010; Feng et al., 2013; Wang et al., 2014, 2018; Jo et al., 2016). DRF associated with BrC is highly uncertain and spans over an order of magnitude from +0.04 to 0.57 W/m^2 (Feng et al., 2013; Lin et al., 2014; Wang et al., 2014). DRE induced by BrC absorption ranges from +0.05 to +0.53 W/m^2 (Wang et al., 2014; Saleh et al., 2015; Jo et al., 2016). More recently, Wang et al. (2018), constraining the model with observations and considering the photochemical whitening due to the ageing of BB BrC (Forrister et al., 2015; Wang et al., 2016), have reduced previous estimates of DRE to +0.048 W/m^2. The magnitude of the calculated effect of BrC on radiation depends on the assumptions made about the sources, ageing processes, and optical properties.

Mineral atmospheric dust particles are emitted by the erosion of wind on the deserts and disturbed soils by anthropogenic activities. Natural dust is emitted in desert and semidesert areas, dry lakes, ephemeral channels, and areas with extreme soil moisture deficits (Choobari et al., 2013). Anthropogenic sources of dust originate from soils disturbed by anthropogenic activities such as vegetation removal, desiccating water bodies, and a changing climate (Tegen et al., 2004; Ginoux et al., 2012). The main sources of dust are located in the Northern Hemisphere near deserts in North Africa, Middle East, and Southwest and East Asia, whereas other smaller sources are located in South Africa, South America, and Australia (Ginoux et al., 2001; Prospero et al., 2002). According to Huneeus et al. (2011), dust emissions estimated by global models span a factor of 5, with a median value of 1,123 Tg/year. The anthropogenic fraction is 20–25% of the total (Ginoux et al., 2012).

Climatic effects associated with dust are complex because it affects the radiation and clouds in multiple ways (Choobari et al., 2013). Aerosol dust acts on the climate directly by scattering and absorbing solar and infrared radiation, semidirectly decreasing cloud cover, and indirectly acting as CCN and IN. Intergovernmental Panel on Climate Change attributed to dust has a global mean RF due to aerosol-radiation interaction between 1,750 and 2,011 of −0.10 W/m^2, with an uncertainty range from −0.3 to +0.1 W/m^2 (Boucher et al., 2013). However, recent studies have reduced the estimated cooling associated with a dust direct effect. Kok et al. (2017) have found that dust in current models is generally too fine relative to the observations. This fact artificially increases the dust cooling effect and underestimates the warming from coarser particles. Moreover, the assumption that dust is spherical leads to the underestimation of the extinction efficiency of larger particles. Using the observations of aerosol abundance and model results to constrain the DRE of dust, Kok et al. (2017) have found a reduction of the cooling effect of about a factor of 2 with respect to AeroCom models. The climatic effect of mineral aerosol also depends on the imaginary part of the refractive index (Pitari et al., 2015). This, in turn, depends on the mineral composition of soils in the source regions. For example, Formenti et al. (2011) showed that the dust from Saleh is redder and more absorbing than Sahara dust. Variation in chemical dust composition may lead to positive or negative RF (Sokolik & Toon, 1999). Scanza et al. (2015) have demonstrated that the inclusion of mineral speciation in the model has the same importance of the assumed dust size distribution. The same authors have shown that including the mineralogy in the model, the RF switches from a small negative (−0.17 and −0.05 W/m^2) value of a reference case to a small positive value (+0.05 W/m^2).

Aerosol DRF and DRE estimates depend critically on many assumptions about the aerosol mass concentration, size, shape, optical properties, and mixing state that affect aerosol optical depth (AOD), single-scattering albedo (SSA), and asymmetry parameter. SSA variations of 11% may change the sign of DRF from negative to positive (Jethva et al., 2014). One of the most uncertain factors in the calculation of AOD and SSA is the assumption of the aerosol mixing state (Curci et al., 2015). Curci et al. (2019) compared an ensemble of regional models over Europe and North America and found that the absolute error in simulating SSA is a few percent, but the sign of the bias has a certain dependence on the aerosol mixing state assumption.

Observations suggest that freshly emitted BC is externally mixed, but it becomes internally mixed with nonabsorbing material with atmospheric ageing (Jacobson, 2000; Cheng et al., 2006; Pratt & Prather, 2010; China et al., 2015; Liu et al., 2017). When BC is coated with nonabsorbing material, its absorption power is amplified through the “lensing effect” (Lesins et al., 2002). The global average BC absorption enhancement factor (E_{abs}) is estimated to be in the range of 1.2–1.6 (Bond et al., 2006; Liu et al., 2017). Recently, Curci et al. (2019) calculated, from an ensemble of models, values of E_{abs} larger than the most accepted upper limit of 1.5. The same authors have shown also that E_{abs} values depend on the mixing assumption made in the model. From a modeling point of view, only the models with a CS treatment for aerosol optical properties may explicitly calculate the E_{abs}, while models with externally mixing assumption use constant values of E_{abs} (e.g., Wang et al., 2014, 2018).

The presence of BrC opens the question about whether it is internally or externally mixed with BC. The mixing state of BrC affects the absorption of both BrC and BC. When BC is coated by a shell containing absorbing material, E_{abs} is affected by the contribution of the lensing effect and shell absorption (Cheng et al., 2017). Cheng et al. (2017) and Luo et al. (2018) have shown that E_{abs} due to lensing decreases when a brown coating is present on the BC core. At the same time, the reduction in lensing may be overcompensated by BrC shell absorption. As a result, E_{abs} may reach values in the range of 2–5 (Cheng et al., 2017; Luo et al., 2018).

In this study, we have used the global chemical and transport model GEOS-Chem (Bey et al., 2001) to perform a multiyear simulation of the radiation-absorbing aerosol (RAA) mass concentration. Starting from the GEOS-Chem output, we have calculated the aerosol optical properties with the FlexAOD postprocessing tool (Curci et al., 2015). RAA mass and their optical properties have been calculated using the most recent updates in terms of ageing, size distribution, and absorption properties inferred from observational constraints. We aimed to study the sensitivity of the absorption properties of carbonaceous aerosol to the mixing state hypothesis and BrC presence. We also explored the sensitivity of the absorption of dust particles to the refractive index and shape. The results obtained in the sensitivity tests were compared with the observations from the Aerosol Robotic Network (AERONET; Holben et al., 2001). Finally, we explored the implications for the resulting DRE.

2. Methods

2.1. GEOS-Chem Model

In this work, we have used the version 11-01 of the GEOS-Chem global chemical and transport model (Bey et al., 2001). We ran the model from 2010 to 2014 with a horizontal resolution of 4° × 5° and 47 vertical levels up to 0.01 hPa. In our work, GEOS-Chem was driven by Modern Era Retrospective-analysis for Research and Application version 2 (MERRA2) assimilated meteorological data from the Global Modelling and Assimilation Office Goddard Earth Observing System (Rienecker et al., 2011). MERRA2 data have a native horizontal resolution of 0.5° lat × 0.625° lon with 72 hybrid sigma/pressure vertical levels and were regridded to the model grid by GEOS-Chem team.

We conducted a full aerosol-oxidant chemistry GEOS-Chem simulation including sulfate, nitrate, ammonium, black carbon, OA, soil dust, and sea salt. Inorganic aerosols were simulated according to Park et al. (2004). The simulation of BC and primary organic aerosol (POA) follows Park et al. (2003). SOAs were parameterized following the work of Pye et al. (2010). Dry deposition used a resistance-in-series model following Zhang et al. (2001). Wet scavenging processes were based on the scheme described by Liu et al. (2001) and included the below-cloud washout from large-scale and convective precipitation, as well as in-cloud removal in both stratiform clouds and convective updrafts.

Primary anthropogenic emissions of BC and POA were taken from the Bond et al. (2007) inventory. Global anthropogenic emissions of CO, NO_x, and SO_x were taken from Emissions Database for Global Atmospheric Research (EDGAR) v4.2 (1° × 1°) (Olivier & Berdowski, 2001), while the volatile organic carbon (VOC) emissions were from the REanalysis of the TROposhperic chemical composition (RETRO) (0.5° × 0.5°) inventory. We used the RETRO inventory for VOCs instead of EDGAR database, because RETRO was considered to have improved temporal and spatial resolution and a more inclusive suite of speciated VOCs than many of the inventories employed in the version of GEOS-Chem used in this work (http://wiki.seas.harvard.edu/geos-chem/index.php/Implementation_of_RETRO_Anthropogenic_Emissions). EDGAR v4.2 data were available for the period 1970–2009, but we did not apply a scaling factor to process the emissions for the years of our simulations (2010–2014). However, where possible, regional inventories were used to replace EDGAR and RETRO. These were EMEP (50 km × 50 km) for Europe, the NEI2011 (12 km × 12 km) for the United States, BRAVO (0.1° × 0.1°) for Mexico, CAC (0.1° × 0.1°) for Canada, and Streets et al. (2006) data (1 km × 1 km) for Asia.

Biogenic emissions were calculated interactively within GEOS-Chem using the Model of Emissions of Gases and Aerosols from Nature (MEGAN) model (Guenther et al., 2006). Soil dust emission was calculated using the Dust Entrainment And Deposition (DEAD) scheme (Zender et al., 2003). Sea salts were emitted in the model using the scheme of Alexander et al. (2005) with the updates introduced by Jaeglé et al. (2011). The BB emissions of BC and POA were taken from GFED4 (Global Fire Emissions Database) inventory (van der Werf et al., 2010; Gilgio et al., 2013).

2.2. Simulation of RAA using GEOS-Chem

GEOS-Chem was modified to include specific treatment of RAAs. The standard model used an ageing lifetime of BC of 1.15 days, and 80% of BC was emitted as hydrophobic. In our work, BC emissions and ageing were source dependent following Wang et al. (2014; 2018). Hydrophobic and hydrophilic BCs were tracked for FF, BF, and BB sources. According to Wang et al. (2014), in our work, 80% of BCs from FF sources were emitted as hydrophobic and converted to hydrophilic with an ageing rate related to sulfate dioxide and hydroxyl radical levels in the atmosphere as in Liu et al. (2011)

$$k = \frac{1}{\tau} = a[SO_2][OH] + b$$

where k and τ are the ageing rate and e-folding time, $a = 2\times10^{-22} \cdot \mathrm{cm}^{-6} \cdot \mathrm{molec}^{-2} \cdot \mathrm{s}^{-1}$ and $b = 5.8 \times 10^{-7} \cdot \mathrm{s}^{-1}$. By contrast, BCs from BF and BB sources were assumed to be emitted as 70% hydrophilic and 30% as hydrophobic with an ageing e-folding time from hydrophobic to hydrophilic of 4 hr. The global emissions of BC were 4.6 Tg/year from anthropogenic sources (3.0 and 1.6 Tg/year from FF and BF, respectively) and 2.0 Tg/year from BB. We have adopted this treatment for BC because it has been shown that it reduces the bias with respect to the observation of BC mass concentration as a result of a shorter lifetime (Wang et al., 2014).

BrC emissions were dominated by primary sources such as BF and BB (e.g., Hecobian et al., 2010; Chen & Bond, 2010), and secondary sources were associated with aromatic carbonyls (X. L. Zhang et al., 2013; Lambe et al., 2010). To our knowledge, no experimental evidence has been reported that POA emitted from FF use is absorbing (Laskin et al., 2015), with the exception of the measurements in Beijing (Yan et al., 2017). BrC was not treated in the current version of GEOS-Chem; therefore, we added four tracers to the model for hydrophobic and hydrophilic BrC from BF and BB sources. At this time, no global emission inventory exists for BrC. Previous studies have assumed that a fraction of POA is emitted as BrC (Feng et al., 2013; Wang et al., 2014). Other studies have estimated the emissions using the relationship between the modified combustion efficiency and absorbing Ångström exponent (Jo et al., 2016) or using the BC/OA ratio (Park et al., 2010; Saleh et al., 2015). In this work, we have used the simple approach adopted by Wang et al. (2014), which assumed that 50% and 25% of POA emitted by BF and BB sources, respectively, is primary BrC. Applying these fractions, POA emissions were split into white POA and BrC at each time step. This results in a global average BrC emission of 7.3 Tg/year (3.1 and 4.2 Tg/year from BF and BB, respectively). Following the treatment of POA in the default model, we have assumed that half of the emitted BrC is hydrophobic, and the conversion of hydrophobic BrC to hydrophilic has an *e*-folding time of 1.15 days. Regarding secondary sources, we treat as absorbing SOA only the aromatic compounds (Wang et al., 2014, 2018; Jo et al., 2016).

Dust emission was simulated using the DEAD scheme (Zender et al., 2003). The dust source function for this parameterization was taken from the Goddard Chemistry Aerosol Radiation and Transport (GOCART) model (Ginoux et al., 2001; Chin et al., 2004). The dust mass in the baseline model was distributed in four standard dimensional bins with diameter boundaries of 0.2–2.0, 2.0–3.6, 3.6–6.0, and 6.0–12.0 μm following the distribution suggested by L. Zhang et al. (2013) that has been evaluated only in the western United States. Recently, Kok et al. (2017) have shown that the brittle fragmentation theory (Kok, 2011) approximates very well worldwide measurements of the emitted dust size distribution. Moreover, Johnson et al. (2012), by applying in GEOS-Chem the distribution of Kok (2011), have found that the model prediction of AOD and extinction is improved. Therefore, in our simulations, we have adopted the distribution of Kok (2011).

A preliminary test conducted with this configuration has returned an average dust atmospheric load of approximately 9 Tg, which is lower than the range of values (13–29 Tg) calculated by Kok et al. (2017) by applying observational constraints. The first explanation for this bias is a low dust emission. It has been known that dust emissions predicted by the DEAD scheme are typically underestimated for coarse grid (4° × 5°) simulation. In our preliminary run, we found a global emission rate approximately 1,120 Tg/year, while the emission calculated at 2°×2.5° is in the range of 1,500–1,700 Tg/year (e.g., Johnson et al., 2012; Ridley et al., 2012). The decrease of dust emissions in the coarse domain of GEOS-Chem in comparison to higher resolution simulations has been studied by Ridley et al. (2013). The authors attributed the bias to the unresolved wind speeds in coarse resolution run due to the averaging of high-resolution winds to lower resolution grids.

Moreover, a qualitative comparison of our preliminary simulation with AOD retrieved by Moderate Resolution Imaging Spectroradiometer (MODIS) has shown the model tendency to underestimate AOD over the Atlantic Ocean across the dust outflow region. A similar behavior has been found with GEOS-Chem by Ridley et al. (2012), and the authors have attributed the bias to an excess of wet removal due to an overestimation of the precipitation rate. Comparing MERRA2 with the Tropical Rainfall Measuring Mission (TRMM) satellite, we have found that the MERRA2 precipitation rate was overestimated in the tropics. Therefore, to correct the precipitation bias and reduce the associated uncertainty in wet deposition, we have scaled the MERRA2 precipitation rate with the average ratio between TRMM and MERRA2 calculated at each grid point. We acknowledge that there exist more refined methods to correct the precipitation bias (e.g., Piani et al., 2010 and references therein). However, for the sake of simplicity, we have adopted this basic approach that adjusts the modeled precipitation rate to the observed long-term averages. After the precipitation rate correction, the comparison with MODIS AOD improves over the Atlantic Ocean, and the average dust atmospheric load is 10 Tg, a value larger than the original (9 Tg) but still lower than the range reported by Kok et al. (2017).

As discussed above, the bias in dust emissions was mainly due to the unresolved wind in the coarse domain. According to Ridley et al. (2013), dust emissions in the coarse domain may be reconciled with higher resolution taking into account the subgrid variability of surface winds, through a Weibull probability distribution. Unfortunately, the method proposed by Ridley et al. (2013) was not implemented in the GEOS-Chem version employed in this work and its implementation was beyond the aim of our study. Therefore, we have scaled the dust emission flux by a constant factor at each grid-point to constrain the global mean dust load to 20 Tg, a value close to the central estimate calculated by Kok et al. (2017). This results in an average emission of approximately 2,300 Tg/year, which is larger than the central estimate (1,700 Tg/year) but lower than the upper limit of 2,700 Tg/year reported by Kok et al. (2017).

2.3. Aerosol Optical Property Calculation

Aerosol optical properties have been calculated from the aerosol mass concentration predicted with GEOS-Chem using the postprocessing tool FlexAOD (Curci et al., 2015, http://pumpkin.aquila.infn.it/flexaod/). FlexAOD has been successfully used in several previous works (Curci et al., 2015, 2019; Jo et al., 2016; Souri et al., 2018; Jin et al., 2019). Here we have focused on BC, BrC, and dust absorption properties. We have conducted a series of numerical experiments aimed at exploring the sensitivity of RAA optical properties to mixing state assumptions, the complex part of the refractive index, and shape.

Aerosol optical properties in FlexAOD are calculated assuming spherical particles using the Mie theory (Mie, 1908). The method used to derive the AOD, SSA, and asymmetry parameters is described in Curci et al. (2015). All aerosol species are assumed to be distributed with a lognormal function, with the exception of dust for which a gamma distribution is employed. A particle density, a dry complex refractive index, and a hygroscopic growth factor are assigned to each aerosol species simulated by GEOS-Chem. The parameters assigned to the RAA aerosol are discussed in the next section.

FlexAOD allows the calculation of aerosol optical properties under different mixing state assumptions. In this work, we used the external mixing and CS internal mixing. In the case of external mixing, the aerosol optical properties were calculated separately for aerosol species simulated by GEOS-Chem and then were summed. For CS internal mixing cases, the volume average refractive index is a function of particle size and is computed before application of the Mie algorithm. The size range spanned by the size distributions of aerosol species was divided into 100-dimensional bins, and the mass of each aerosol species was calculated in each bin. The mass was then converted to volume dividing by the species density, and the average refractive index in each size bin was calculated using the species volume as the weighting factor. For the CS assumption, the refractive index was calculated for a core (black carbon) and for a homogeneously mixed shell (nonblack carbon species). Mie calculations were performed using the code based on Mishchenko et al. (1999) for external mixing, and the code based on Toon and Ackerman (1981) for the CS internal mixing. A more detailed description of FlexAOD is reported in the supporting information.

2.4. Treatment of RAA Optical Properties

In this work, the size distribution parameters of BC are source dependent and follow Wang et al. (2014). The geometrical median radius was set to 30 and 70 nm for FF and BF/BB black carbon, while the standard deviations were 1.4 and 1.6, respectively. The refractive index was 1.95–0.79i, as recommended by Bond and Bergstrom (2006). The BC density was assumed to be 1.8 g/cm^3.

The geometrical median radius, standard deviation, and density of BrC are the same one employed by Wang et al. (2018) for OA, their values being 90 nm, 1.6 and 1.3 g/cm^3, respectively. The real part of BrC refractive index is the same of nonabsorbing OA, and it was taken from the Optical Properties of Aerosol and Cloud (OPAC) database (Hess et al., 1998). The imaginary part has been inferred starting from the mass absorption coefficients (MACs) of BF and BB absorbing OA recommended by Wang et al. (2018). Their MAC$_{OA}$ is based on the laboratory study of Saleh et al. (2014) and was constrained by aircraft observations in the United States. We have adopted MAC$_{OA}$ of Wang et al. (2018) since, to our best knowledge, they are only optimized from atmospheric measurement constraints. MAC$_{OA}$ at 440 nm assigned to BF was 0.76 m^2/g. To include the photochemical whitening of BB, we have adopted two different MAC$_{OA}$ values for fresh and aged plumes. For freshly emitted (hydrophobic) BB, MAC$_{OA}$ at 440 nm recommended by Wang et al. (2018) is 0.77 m^2/g. Concerning the aged BB, the blanching process may be simulated by tracking the absorption in the model or by reducing the MAC$_{OA}$. We have adopted the second solution because we have tracked the aged (hydrophilic) BrC, and because it is more practical for a postprocessing calculation. Following again Wang et al. (2018), the MAC$_{OA}$ value at 440 nm for aged BB adopted here is 0.23 m^2/g.

Knowing the contribution of BrC to OA, the MAC$_{OA}$ may be translated to MAC$_{BrC}$ using equation 2 of Wang et al. (2018):

$$\mathrm{MAC_{OA}} \cdot \mathrm{Mass_{OA}} = \mathrm{MAC_{BrC}} \cdot \mathrm{f} \cdot \mathrm{Mass_{OA}}$$

where *f* is the fraction of OA mass that is BrC. In our case, BrC contributed to 50% and 25% of the BF and BB OA, respectively. MAC$_{BrC}$ at 440 nm and the relative complex part of the refractive index calculated from this are reported in Table 1. MAC$_{BrC}$ from BF was 1.56 m^2/g, while those of freshly and aged BB was 3.08 and 0.92 m^2/g. The resulting MAC$_{BrC}$ values were in the range of 0.63–1.6 m^2/g at 450 nm used by Feng et al. (2013), with the exception of MAC$_{BrC}$ for fresh BB, which is approximately 2 times larger than the upper limit of Feng et al. (2013) but comparable to the MAC$_{BrC}$ of 3.34 m^2/g at 405 nm applied by Jo et al. (2016). Finally, BrC from secondary sources was assumed to have the same size distribution of primary BrC and have attributed it at a MAC$_{BrC}$ of 0.3 m^2/g at 440 nm as in Wang et al. (2014). It should be noted

Table 1
Mass Absorption Coefficient (MAC) and Refractive Index of BrC at 440 nm Used in This Work for Biofuel, Fresh, and Aged Biomass Burning OA and BrC

Source	MAC_{OA}[a] (m^2/g)	MAC_{BrC}[b] (m^2/g)	BrC refractive index[c]
Biofuel	0.76	1.56	1.54–0.071*i*
Fresh biomass burning	0.77	3.08	1.54–0.140*i*
Aged biomass burning	0.23	0.92	1.54–0.042*i*
Feng et al. (2013; 450 nm)	0.41–1.06[d]	0.63–1.6	0.063–0.02
Jo et al. (2016; 405 nm)	-	3.34	0.14

Abbreviations: BB: biomass burning; BF: biofuel; BrC: brown carbon; OA: organic aerosol.
[a] Wang et al. (2018). [b] MAC_{OA} has been transferred to MAC_{BrC} with the equation 2 of Wang et al. (2018) (see section 2.4) using the BrC contribution to OA of 50% and 25% from BF and BB sources, respectively. [c] The complex part is derived from $(MAC \cdot \rho \cdot \lambda)/4\pi$, where ρ is the density of BrC (1.3 g/cm^3). [d] Feng et al. (2013) assumed that 66% of OA from BF and BB is BrC.

that MACs for absorbing OA reported by Wang et al. (2018) have been optimized based on regional observations in the United States. Therefore, BrC properties were not consistent in other regions.

As discussed in section 2.2, dust size distribution was simulated over four-dimensional bins. For optical calculations, the finer bin was split into four bins following Ridley et al. (2012). The mass fraction attributed to each dimensional bin is reported in Table 2. Dust bins were assumed to be distributed over the same gamma distribution, but they contribute to the optical calculations in limited size ranges, as indicated in Table 2. The refractive index used for dust particles is discussed in the next section.

2.5. Numerical Experiments

A series of numerical experiments has been conducted with FlexAOD to test the sensitivity of aerosol-absorbing properties to the mixing state, dust refractive index, and shape. The list of our sensitivity simulations is reported in Table 3.

The first experiment assumes that aerosols are externally mixed and that OA is nonabsorbing. This simulation was our reference case (CTRL). In the next two experiments, BC is considered internally mixed. A classic way to represent the internal mixing of BC is the CS assumption (Jacobson, 2001; Bond & Bergstrom, 2006), where a core made of BC is coated by a shell of nonabsorbing material. In the second test (CS-BC), we consider the BC internally mixed with sulfate-ammonium-nitrate and OA, while dust and sea salt are assumed to be mixed externally. In the real atmosphere, observations of the mixing state indicate that BC is externally mixed close to the sources, while coating with the inorganic aerosols and OA is found for aged BC (Jacobson, 2000; Cheng et al., 2006; Pratt & Prather, 2010; China et al., 2015; Liu et al., 2017). Therefore, a partial internal mixing (PIM) for the particles is the most likely mixing state of aerosols. PIM could be implemented calculating the fraction of internally mixed particles by using the parameterization of Cheng et al. (2012), as reported by Curci et al. (2019). However, because GEOS-Chem simulates separately the fresh and aged BC and POA, in the third experiment (PIM-BC), we considered only the aged BC as internally mixed, while freshly emitted BC and POA (hydrophobic) were considered externally mixed with dust and sea salt. In both CS-BC and PIM-BC experiments, OA was not considered absorbing.

The contribution of BrC to aerosol absorption was considered in the next experiments. CTRL, CS-BC, and PIM-BC were repeated including the absorption of OA, as described in section 2.4. These simulations were labeled EXT-BrC, CS-BrC, and PIM-BrC. It should be noted that freshly emitted BC displays a fractal

Table 2
Dust Size Distribution Used for Optical Calculation

GEOS-Chem dust size distribution[a]	**Bin 1** (0.2–2.0 μm)				**Bin 2** (2.0–3.6 μm)	**Bin 3** (3.6–6.0 μm)	**Bin4** (6.0–12 μm)
Fraction[b]	0.06	0.12	0.24	0.58	1.0	1.0	1.0
Size range[c] (μm)	0.2–0.36	0.36–0.6	0.6–0.96	1.3–2.0	2.6–3.6	4.4–6.0	7.0–12.0

[a] Dimensional bins used by GEOS-Chem to simulate the dust size distribution (see section 2.3). [b] Mass fraction attributed to each dimensional subbin of the finest bin (Ridley et al., 2012). [c] Dust is distributed following a gamma function $N(r) = N_0 r^{(1-3b)/b} \exp\left(-\frac{r}{ab}\right)$ (a=0.9, b=0.2). Each bin contributes to the optical calculations in a limited size ranges as indicated in the table.

Table 3
Summary of the Numerical Experiments Conducted with FlexAOD

Experiment	Externally mixed	Internally mixed	BrC
CTRL	All	-	-
CS-BC	Dust, sea salt	BC core, sulfate-ammonium-nitrate and all OA in the shell	-
PIM-BC	Dust, sea salt, freshly emitted BC and POA	BC core, sulfate-ammonium-nitrate, aged POA and SOA in the shell	-
EXT-BrC	All	-	Yes
CS-BrC	Dust, sea salt	BC core, sulfate-ammonium-nitrate and all OA in the shell	Yes
PIM-BrC	Dust, sea salt, freshly emitted BC and POA	BC core, sulfate-ammonium-nitrate, aged POA and SOA in the shell	Yes
DUST-L	Low absorption, dust refractive index from Sinyuk et al. (2003)		
DUST-M	Mid absorption, dust refractive index from Petzold et al. (2009)		
DUST-H	High absorption, dust refractive index from Wagner et al. (2012)		
DUST-NS	As DUST-L, but for nonspherical dust particles		

Abbreviations: AOD: aerosol optical depth; BC: black carbon; BrC: brown carbon; CS: core-shell; OA: organic aerosol; PIM: partial internal mixing; POA: primary organic aerosol.

structure that becomes more compact during ageing (China et al., 2013; Wang et al., 2017). Here we assume that the fractal aggregates of freshly emitted BC have already collapsed in a compact and spherical cluster.

One of the main uncertainties in dust particle absorption properties is related to the uncertainties in the imaginary part of the refractive index (Sokolik & Toon, 1999; Pitari et al., 2015; Scanza et al., 2015), which depends on the mineral composition of dust particles. Here we test the sensitivity of dust absorption to three different refractive index databases that we classify as “low,” “middle,” and “high” absorption. For low (DUST-L), middle (DUST-M), and high (DUST-H) absorption, the refractive indices were taken from Sinyuk et al. (2003), Petzold et al. (2009), and Wagner et al. (2012), respectively. These databases have a spectral dependence covering the entire spectrum. The imaginary part reported by Sinyuk et al. (2003) is 0.0014 at 550 nm. Petzold et al. (2009) have shown a value about 2 times larger than that of Sinyuk et al. (2003; 0.0028 at 550 nm). Wagner et al. (2012) estimated a value of 0.0055 at the same wavelength. For dust experiments, we considered the DUST-L simulation as the reference case.

Finally, we studied the impact of the nonspherical particles assumption on dust absorption (DUST-NS). The extinction efficiency, SSA, and asymmetry parameters for nonspherical particles are calculated with the T-matrix code for randomly oriented, nonspherical particles (Mishchenko et al., 1996; Mishchenko & Travis, 1998). Dust nonspherical particles are considered as oblate spheroids with an aspect ratio of 1.7. In DUST* experiments, dust particles were assumed to be externally mixed with an external mixture of sea salt, freshly emitted BC and BrC, and with an internal mixture composed by a core of aged BC coated by inorganic aerosols, nonabsorbing OA, and aged BrC (i.e., DUST-L and PIM-BrC are equivalent).

2.6. Radiative Transfer Model

We calculated the shortwave (SW) DRE at the top of the atmosphere (TOA) by BC and dust for the experiments listed in Table 3 using the Rapid Radiative Transfer Model for General Circulation Models (RRTMG; Iacono et al., 2008), following Jo et al. (2016). RRTMG has also been used to calculate the dust DRE TOA for longwave (LW) radiation. Monthly AOD, SSA, and asymmetry parameters used for the DRE estimate were calculated using FlexAOD, as detailed in the previous section. Monthly temperature, water vapor, cloud liquid and ice water path, cloud fraction, surface albedo for direct and diffuse radiation in visible and near-infrared bands, and surface emissivity were taken from MERRA2 reanalysis. Tropospheric and stratospheric ozones were taken from the GEOS-Chem output. Cloud droplet and ice crystal effective radii were from monthly MODIS-Aqua cloud products. Greenhouse gases (CO_2, CH_4, N_2O, CFC-11, CFC-12, CFC-22, and CCl4) were fixed to the climatological mixing ratios.

2.7. AERONET Measurements

We used Sun photometer observations from the AERONET (Holben et al., 2001) for the years 2010–2014 to evaluate the aerosol absorption properties calculated with FlexAOD. AERONET provides worldwide observations of the AOD, SSA, and asymmetry parameters at several wavelengths (440, 675, 870, and 1,020 nm). AERONET observations include two levels of data, the cloud-screened and quality-assured L2.0 (Dubovik et al., 2002) and cloud-screened L1.5. In L2.0, SSA is available only for high AOD values (AOD>0.4 at 440 nm). As a result, this subset is only 20% of the L1.5 data related to absorption retrieval (Wang et al., 2016). Thus, as in Wang et al. (2016) and Curci et al. (2019), we have complemented the L2.0 dataset for SSA with L1.5. The fraction of data from L2.0 (Figure S1 in the supporting information) used in this study is below 10–20% in North America and Europe, and it is larger than 40% only for some stations located in Arabian Peninsula, India, and Eastern China. The highest aerosol absorption values are found at stations with larger coverage of L2 data (Figure S2).

AERONET absorption includes the contribution of BC, BrC, and dust. To isolate the contribution to the absorption of a given species, we have selected the AERONET scenes classified as “BC-dominated,” “BC+BrC-dominated,” and “Dust-dominated,” following the criteria suggested by Bahadur et al. (2012). We define

$$\mathrm{AAOD}_\lambda = \mathrm{AOD}_\lambda\cdot(1-\mathrm{SSA}_\lambda)$$

$$\mathrm{SAOD}_\lambda = \mathrm{AOD}_\lambda\cdot\mathrm{SSA}_\lambda$$

$$\mathrm{SAE}_{440}^{675} = -\frac{\ln(\mathrm{SAOD}_{440}/\mathrm{SAOD}_{675})}{\ln(440/675)}$$

$$\mathrm{AAE}_{440}^{675} = -\frac{\ln(\mathrm{AAOD}_{440}/\mathrm{AAOD}_{675})}{\ln(440/675)}$$

where SAOD and AAOD are the scattering and absorption AODs and SAE and AAE are the scattering and absorption Ångström exponents, respectively. Following Bahadur et al. (2012), Dust-dominated scenes exhibit SAE≤1.2. The remaining scenes are considered as “dust-free,” and the absorption is dominated by carbonaceous aerosols. In particular, BC-dominated scenes have SAE>1.2 and AAE<1.2, while the remaining cases are “BC+BrC-dominated.” It should be noted that the criteria for Dust-dominated scenes was issued with regional measurements from sites located in Sahara and Arabian Peninsula; therefore, it could not be consistent in other locations dominated by dust absorption.

In this work, we have used only the AERONET sites having at least 10% of data coverage in the period 2010–2014, for a total of 90 stations. Figure 1 shows the maps of the stations used for each absorbing scene and the relative fraction of the three absorption classes for each sites.

3. Results

The results of each experiment performed with FlexAOD have been compared with the aerosol optical properties retrieved at AERONET stations. Aerosol optical properties were calculated from the three hourly GEOS-Chem output, for all AERONET observations within ±1 hr with respect to the model. A series of statistical indices have been used to compare the simulation skill in reproducing the observations. These include the observed and modeled mean, fraction of modeled values within a factor of 2 of the observations (FAC2), mean bias (MB), normalized mean bias (NMB), and Pearson correlation coefficient. They are defined in Appendix A. The comparison between the observed and predicted absorption properties was performed separately for BC-dominated, BC+BrC-dominated, and Dust-dominated scenes only for the AAOD. The statistical scores obtained for AAOD, SSA, and the AAE are reported in Tables 4, 5, and 6, respectively.

Before the comparison against the observed absorption properties, we have evaluated the model performance in calculating the AOD at 440 and 675 nm observed by AERONET Sun photometers. In the PIM-BrC experiment (Figure S3 and Table S1 in the supporting information), AOD was reproduced with a correlation of 0.90 and 0.86 at 440 and 675 nm, respectively. The NMB was −18% and −25% for the same variables. These scores reflected the model skill in reproducing the aerosol load, which depends on several

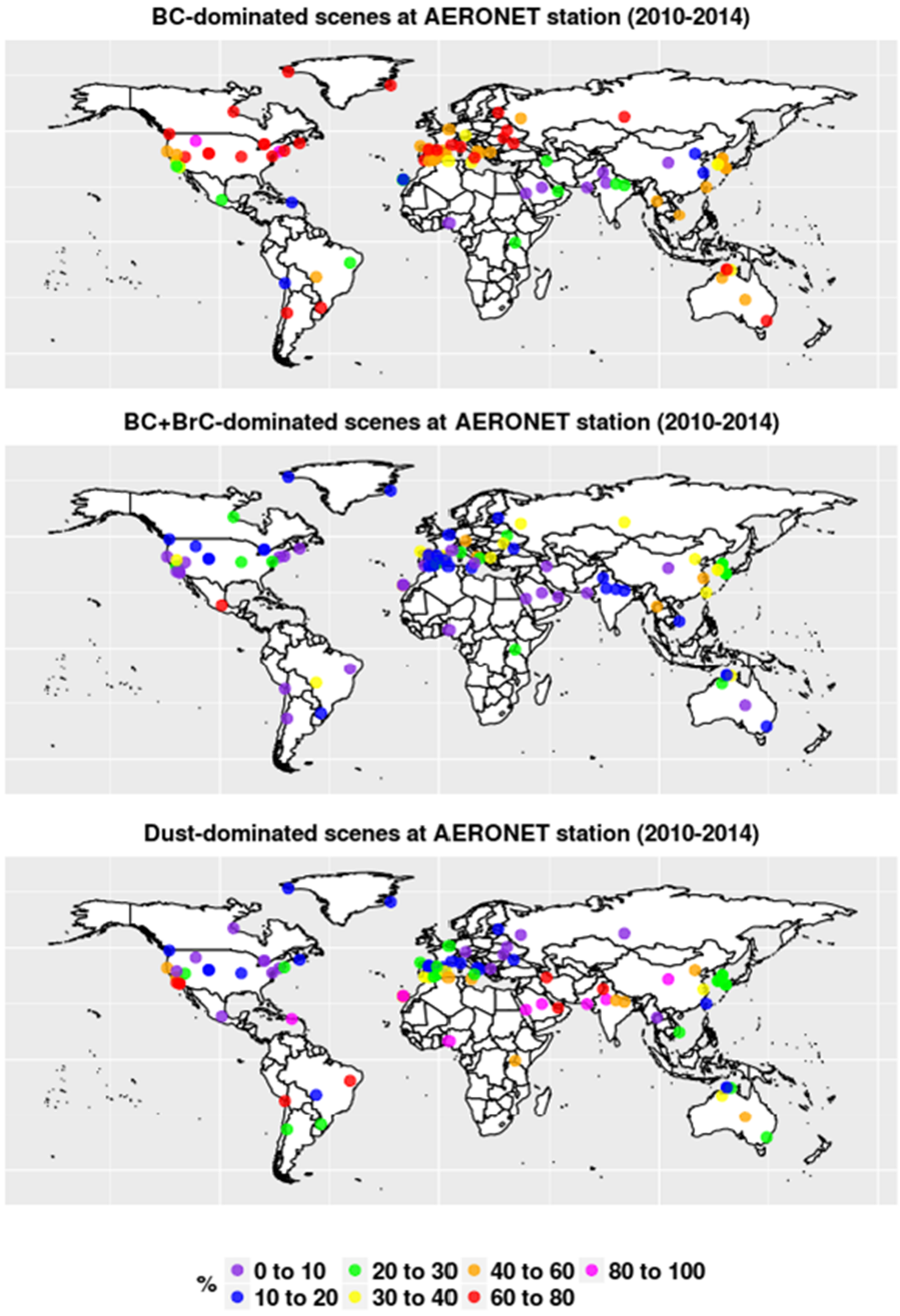

Figure 1. Maps of the Aerosol Robotic Network (AERONET) stations used for each absorbing scene (BC-dominated, BC+BrC-dominated, and Dust-dominated) and the relative fraction of the three absorption classes for each sites.

processes (emissions, transport, and deposition). Statistical scores were almost the same for all simulations, because the AOD is mainly determined by aerosol mass and only secondarily affected by the mixing state (Curci et al., 2019).

Figure 2 shows the scatterplots of 2010–2014 averages of the observed and simulated AAOD at 440 nm, for the most representative experiments (CTRL, PIM-BC, EXT-BrC, and PIM-BrC) for the scenes dominated by

Table 4
Comparison of the Modeled and Observed AAOD at 440 nm for the Period 2010–2014 at AERONET Stations

Experiment	O	M	FAC2	MB	NMB (%)	*r*
BC-dominated scenes						
CTRL	0.016	0.005	0.31	−0.010	−66	0.64
CS-BC	0.016	0.009	0.64	−0.007	−43	0.71
PIM-BC	0.016	0.009	0.58	−0.007	−46	0.72
EXT-BrC	0.016	0.007	0.48	−0.009	−56	0.73
CS-BrC	0.016	0.015	0.85	−0.001	−4.0	0.78
PIM-BrC	0.016	0.014	0.84	−0.002	−14	0.78
BC+BrC-dominated scenes						
CTRL	0.025	0.007	0.17	−0.018	−72	0.70
CS-BC	0.025	0.012	0.38	−0.013	−53	0.76
PIM-BC	0.025	0.011	0.33	−0.014	−55	0.77
EXT-BrC	0.025	0.009	0.28	−0.016	−64	0.75
CS-BrC	0.025	0.020	0.75	−0.005	−20	0.79
PIM-BrC	0.025	0.018	0.71	−0.007	−29	0.79
Dust-dominated scenes						
DUST-L	0.022	0.019	0.79	−0.003	−14	0.82
DUST-M	0.022	0.023	0.74	+0.001	+6.1	0.82
DUST-H	0.022	0.027	0.71	+0.005	+23	0.80
DUST-NS	0.022	0.019	0.79	−0.002	−11	0.82

Note. The experiment list is reported in Table 2.
Abbreviations: AAOD: absorption aerosol optical depth; AERONET: Aerosol Robotic Network; BC: black carbon; BrC: brown carbon; CS: core-shell; MB: mean bias; NMB: normalized mean bias; PIM: partial internal mixing.

BC absorption. The model correlation with observations ranged from 0.64 (CTRL) to 0.78 (CS-BrC and PIM-BrC). As expected, the reference case exhibited the lower performance in reproducing the observed AAOD. The retrieved AAOD was underestimated by −66%, and only 31% of the modeled values were within a factor of 2 with respect to the observations. In the CS-BC case, FAC2 increased to 0.64 and the model underestimation decreased by 35% with respect to CTRL simulations. PIM-BC showed similar results to CS-BC, and the average AAOD was slightly lower than that of CS-BC. Including the OA absorption in an externally mixed state (EXT-BrC), the MB decreased by 15% with respect to the reference case. The model correlation with AERONET data reached the maximum value (0.78) when BrC was considered internally or partial internally mixed. In these experiments, FAC2 was around 0.85 and the model bias values were −4% and −14% for CS-BrC and PIM-BrC, respectively. Including the absorbing shell in the simulation, the model MB was lowered by a factor of 7 with respect to the CS cases with non-absorbing OA.

Figure 3 displays the comparison between the observed and simulated AAOD at 440 nm but for the BC+BrC-dominated scenes. The CTRL run exhibits a correlation of 0.70, a bias of −72%, and only 17% of the simulated sample within a factor 2 of observations. When the CS morphology is considered, the model correlation increased to 0.76 and the observed AAOD was underestimated by about a factor of 2 in both CS-BC and PIM-BC experiments. Considering the BrC absorption in the model, the simulation results improved. The correlation and MB for EXT-BrC were 0.75 and −64%, respectively. The model correlation increased to 0.79 in the CS-BrC and PIM-BrC experiments. The MB values were −20% and −29% for CS-BrC and PIM-BrC, respectively. In both simulations, more than 70% of the simulated values are within a factor of 2 with respect to the AERONET data. The sources of bias affecting our results are discussed in section 4.

E_{abs} has been estimated as the ratio between the AAOD obtained in CS* and PIM* and that calculated in the CTRL case, once the contribution of the dust particles has been subtracted. In the experiment with CS-BC, E_{abs} values were 1.9 and 1.8 for BC- and BC+BrC-dominated scenes, respectively. When the PIM state was assumed, these values decreased to 1.8 and 1.7, respectively. Considering the OA absorption, the E_{abs} values in CS-BrC were 3.4 and 3.2 for BC- and BC+BrC-dominated scenes, respectively, while they were lowered to 3.1 and 2.8, respectively, in the PIM-BrC simulations. We noticed that E_{abs} calculated in PIM-* was approximately 10% lower than that inferred from CS-* simulations.

Table 5
Comparison of the Modeled and Observed SSA at 440 nm for the Period 2010–2014 at AERONET Stations

Experiment	O	M	FAC2	MB	NMB (%)	*r*
CTRL	0.914	0.964	1	0.050	5.5	0.23
CS-BC	0.914	0.943	1	0.030	3.3	0.32
PIM-BC	0.914	0.947	1	0.034	3.7	0.33
EXT-BrC	0.914	0.955	1	0.041	4.5	0.30
CS-BrC	0.914	0.909	1	−0.005	−0.55	0.35
PIM-BrC	0.914	0.918	1	0.004	0.45	0.31
DUST-L	0.914	0.918	1	0.004	0.45	0.31
DUST-M	0.914	0.910	1	−0.003	−0.35	0.30
DUST-H	0.914	0.904	1	−0.009	−1.0	0.26
DUST-NS	0.914	0.916	1	0.003	0.35	0.31

Abbreviations: AERONET: Aerosol Robotic Network; BC: black carbon; BrC: brown carbon; CS: core-shell; MB: mean bias; NMB: normalized mean bias; PIM: partial internal mixing.

E_{abs} estimated for BC with a nonabsorbing coating was comparable to or above the upper limit of ≈1.5 recommended by Bond et al. (2006). By contrast, when BC was coated by absorbing OA, the E_{abs} was approximately 2 times larger than the accepted upper limit. However, at the same time, it was within the measured range of 1–3.5 reported in some studies (e.g., Khalizov et al., 2009; Bond et al., 2013). Furthermore, the E_{abs} estimated by our model was lower than the range of 3.85–5.80 at 404 nm calculated for thickly coated BC by Luo et al. (2018). The discrepancy was most likely due to that reported by Luo et al. (2018), in which the coating was only constituted by BrC without including inorganic aerosol, and BrC imaginary part of the refractive index was different.

Figure 4 displays the comparison of AAOD at 440 nm at the AERONET stations dominated by dust absorption. The DUST-L

Table 6
Same as in Table 6 but for AAE Between 440 and 675 at AERONET Stations

Experiment	O	M	FAC2	MB	NMB(%)	*r*
CTRL	1.18	1.15	1	−0.015	−1.3	0.50
CS-BC	1.18	1.50	1	0.33	28	0.54
PIM-BC	1.18	1.44	1	0.28	23	0.57
EXT-BrC	1.18	1.68	0.99	0.50	43	0.53
CS-BrC	1.18	2.67	0.21	1.5	125	0.31
PIM-BrC	1.18	2.51	0.31	1.3	114	0.44

Abbreviations: AAE: absorption Ångström exponent; AERONET: Aerosol Robotic Network; BC: black carbon; BrC: brown carbon; CS: core-shell; MB: mean bias; NMB: normalized mean bias; PIM: partial internal mixing.

experiment exhibited a correlation of 0.82, a MB of −14%, and a FAC2 of 0.79. Although the comparison was reasonable in terms of bias, the dust particle contribution to the total absorption was 30%, indicating that the modeled absorption was not dominated by dust, as well as in the observations. In the middle dust absorption simulation (DUST-M), AAOD increased by 21% with respect to the low absorption case, and dust particles contributed 55% of the total aerosol absorption. In the high-scenario absorption (DUST-H), the modeled AAOD increased by 42% with respect to DUST-L, and dust AAOD was 70% of the total absorption. Although dust absorption increased in the last two simulations, it should be noted that the modeled AAOD values were overestimated by 6% and 23% and the FAC2 values were 0.74 and 0.71 for DUST-M and DUST-H simulations, respectively. Considering the nonspherical shape (DUST-NS), the dust absorption increased by 5% with respect to DUST-L, suggesting a relatively minor role played by the spherical assumption in the total uncertainty.

Figure 5 shows the scatter plots between the observed and simulated SSA at 440 nm for the most representative experiments. In the CTRL case, SSA was reproduced with a correlation of 0.23 and was overestimated by 5.5%. When the aerosol particles were considered internally mixed, the model bias in reproducing SSA

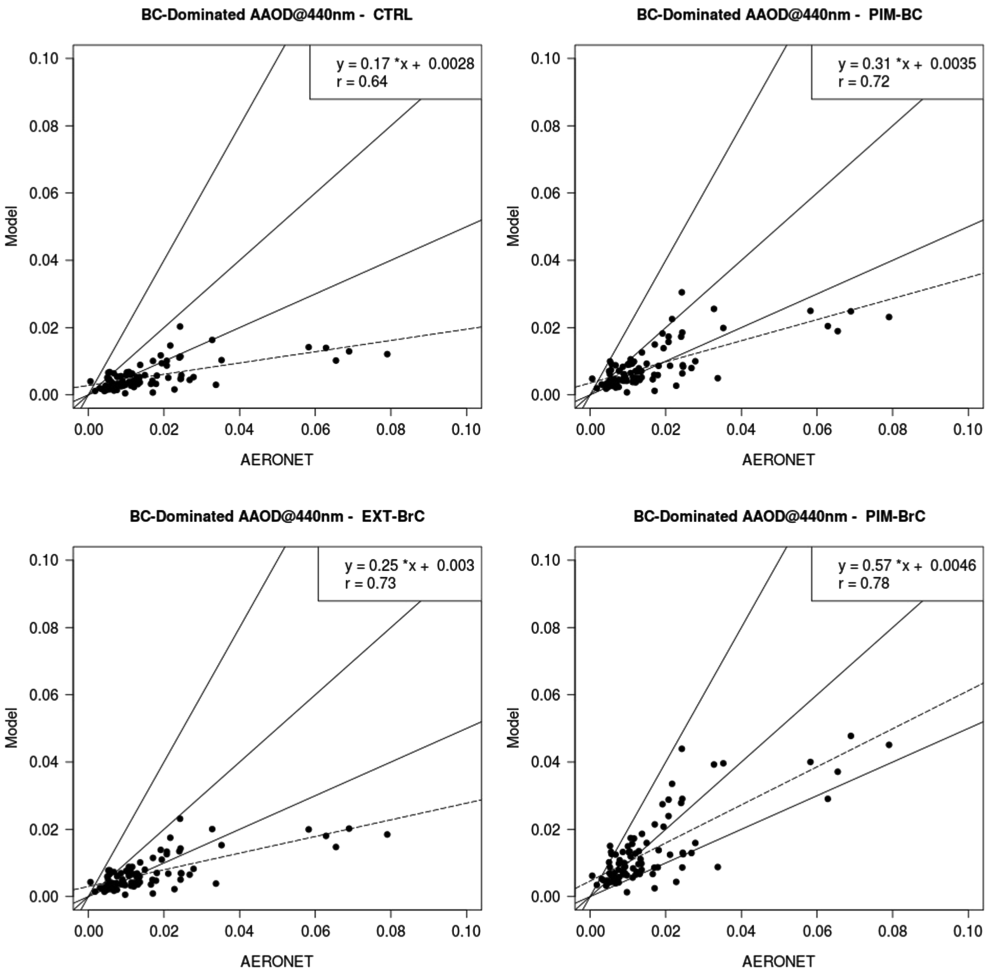

Figure 2. Comparison of the observed and most representative FlexAOD simulations (CTRL, PIM-BC, EXT-BrC, and PIM-BrC) of the average absorption aerosol optical depth (AAOD) at 440 nm for the period 2010–2014 at Aerosol Robotic Network (AERONET) stations for the BC-dominated scenes. The simulations are described in Table 3.

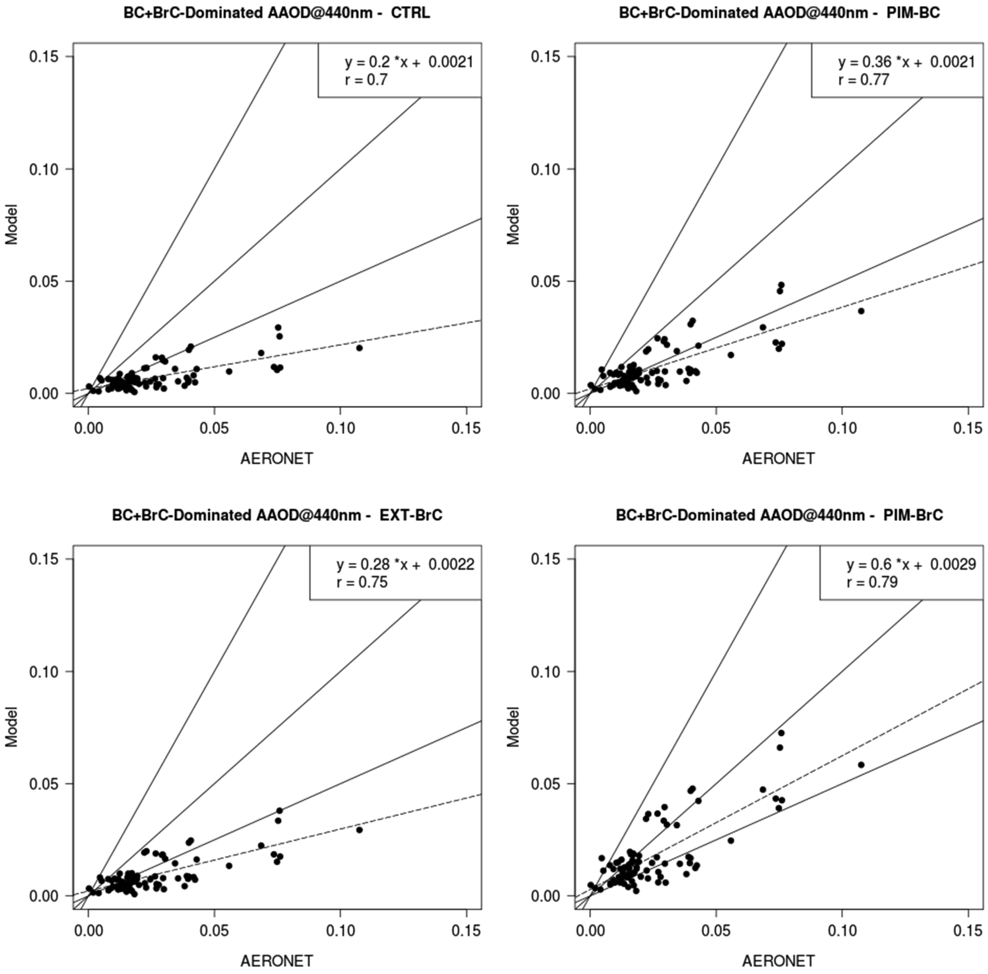

Figure 3. Same as Figure 1 but for BC+BrC-dominated scenes.

decreased to +3.3% and +3.7% in CS-BC and PIM-BC, respectively. Including the absorption from BrC in an external mixing approach (EXT-BrC), the model correlation increased to 0.30 and the bias was lowered to 4.5% with respect to CTRL. When BC was coated or partially coated by absorbing OA, the overestimation

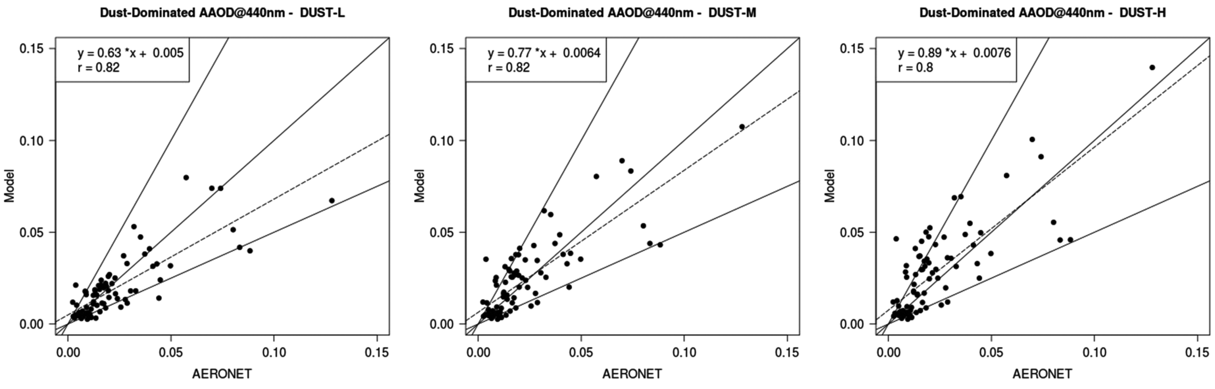

Figure 4. Comparison of the observed and most representative FlexAOD simulations (DUST-L, DUST-M, and DUST-H) of the average absorption aerosol optical depth (AAOD) at 440 nm for the period 2010–2014 at Aerosol Robotic Network (AERONET) stations for the Dust-dominated scenes. The simulations are described in Table 3.

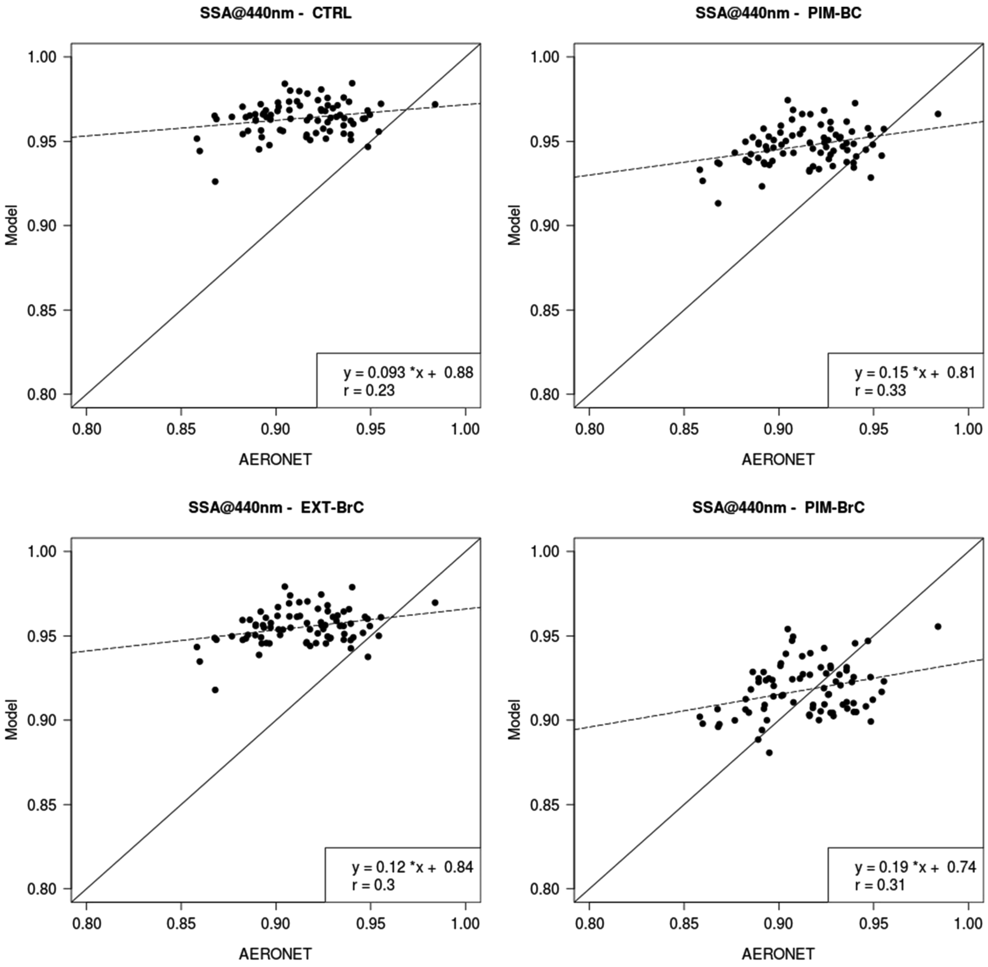

Figure 5. Comparison of the observed and most representative FlexAOD simulations (CTRL, PIM-BC, EXT-BrC, and PIM-BrC) of the average single-scattering albedo (SSA) at 440 nm for the period 2010–2014 at Aerosol Robotic Network (AERONET) stations.

of AERONET retrieval decreased with respect to the experiments discussed. The NMB values were −0.55% and +0.45% for CS-BrC and PIM-BrC, respectively.

As discussed in the section 2.7, we have complemented the L2.0 of AERONET dataset for SSA with L1.5 measurements, since SSA in L2 was provided only for AOD at 440 nm larger than 0.4. It should be noted that the uncertainty associated to SSA retrieval increased from ±0.03 for AOD at 440 nm larger than 0.5 to ±0.05–0.07 for AOD less than 0.2 (Dubovik et al., 2002). In order to explore the impact of uncertainties in retrieved SSA on model validation, we have evaluated our simulations with SSA associated to AOD at 440 nm larger than 0.15. We have chosen this threshold since it is the median of the observed AOD, larger values would drastically reduce the available sample. Scatter plots of the comparison for the most representative cases are shown in Figure S4, and the statistical scores are summarized in Table S2. Model performances looked better with respect to the comparison performed using all observed AOD data. The model correlation with measurements ranged from 0.32 of CTRL case to values larger than 0.50 for CS* and PIM* experiments. Also, the biases were lower with respect to the analysis done without applying any threshold to AOD values. These results indicated that uncertainty in SSA associated with low AOD conditions likely affected the comparison between modeled and observed SSA.

Increasing dust particle absorption, the model correlation with observations was 0.30 and 0.26 for DUST-M and DUST-H simulations, and the SSA values were underestimated by 0.35 and 1.0%, respectively, in the same experiments. Considering the nonspherical shape of dust particles (DUST-NS), the bias was decreased by 0.1% with respect DUST-L experiment. Also, in this case, taking into account only the AOD, larger 0.15 model correlation increases to 0.51 and 0.30 in DUST-L and DUST-H experiments.

Finally, we focused on the AAE between 440 and 675 nm. The comparison of the simulations with the observed AAE was useful to explore the spectral dependence of the absorption in the various experiments. AAE was overestimated in all our simulations, with the exception of CTRL. The average observed AAE was 1.2, which is a typical value when the absorption was dominated by the coated BC (Liu et al., 2018). The modeled AAE in the CTRL was 1.2 and increased to 1.5 and 1.4 in PIM-BC and CS-BC experiments, respectively, indicating that the absorption decreased more rapidly than CTRL with the wavelength. In fact, although the AAOD at 675 nm was simulated with a correlation of about 0.76, it was underestimated by 40–50% in CS* and PIM* simulations (Figure S5 and Table S3). Considering the OA absorption, AAE further increased to 1.7, 2.7, and 2.5, highlighting a more important impact of BrC on the absorption with respect to the observations. AAE overestimation after the inclusion of BrC was also reported in previous works (Wang et al., 2014; Jo et al., 2016; Curci et al., 2019). The modeled AAE values suggested a smaller contribution of BC to the absorption with respect to those retrieved from AERONET Sun photometers. The experiments concerning dust absorption did not show a particular sensitivity in terms of AAE.

4. Discussion of Uncertainties

In summary, the BC absorbing properties are sensitive to the aerosol mixing state assumptions and the presence of BrC. A common feature for all simulations involving the carbonaceous aerosol is a negative bias of the absorption and an underestimation of the BC contribution to the total absorption (AAE is overestimated).

The biases could be related to the uncertainties of BC emissions from both biomass and anthropogenic sources. For example, the anthropogenic emissions from Bond et al. (2007) were not for the simulation years and the use of newer inventories is desirable. In our work, we found the largest negative bias in the absorption (up to −50%) in the regions dominated by BB (not shown). This is consistent with Bond et al. (2013) and with the results discussed by Jo et al. (2016) and Wang et al. (2014). According to the same authors, the anthropogenic emission uncertainties could impact the simulation of BC absorption. Wang et al. (2014), increasing the BF emissions by 30% over Europe, found an improvement in the AAE simulation. Jo et al. (2016), increasing the BC emissions as suggested by top-down estimates, showed a better agreement with AAE observations.

The spherical shape assumption for fractal aggregates of freshly emitted BC could introduce large errors in the calculation of absorbing optical properties. The homogeneous sphere approximation for BC fractal aggregates underestimates MAC below 550 nm (Scarnato et al., 2013). For example, He et al. (2015) found that assuming a volume-equivalent BC sphere instead of fractal aggregates decreased the absorption of freshly BC by 5–25%. On the other hand, SSA at 525 nm for lacy soot calculated using Mie algorithm could differ up to 149% with respect to the SSA estimated from fractal aggregates (China et al., 2015).

Another factor affecting the BC absorption is the CS model. Really, the absorption enhancement for aged BC depends on the position of BC aggregate with respect to the coating material (Scarnato et al., 2013). The absorption cross section of coated BC may increase by 20–250% depending on coating structure and morphology (He et al., 2015). According to Luo et al. (2018), the CS model underestimates the absorbing cross section of thinly coated BC in the ultraviolet region but overestimates it in the visible band. By contrast, the absorbing cross section of thickly coated BC is underestimated at all wavelengths by the CS model for small values of the BrC refractive index. Consequently, a model more accurate than the CS, including the BC morphology in the calculation of the mixing state, is desirable. An example of such a model is the multiple-sphere T-matrix (X. L. Zhang et al., 2017) as suggested by Luo et al. (2018).

Another critical point is the assumption about the BC size distribution. Curci et al. (2019), increasing the typical radius adopted for BC (0.02 μm), found an AAE more comparable with the observed values, highlighting the need to consider a time-dependent size distribution.

In addition, the role of BrC could be underestimated because we considered as BrC sources POA emitted from BF and BB combustions and aromatic SOA, but FF OA could be light absorbing (Yan et al., 2017)

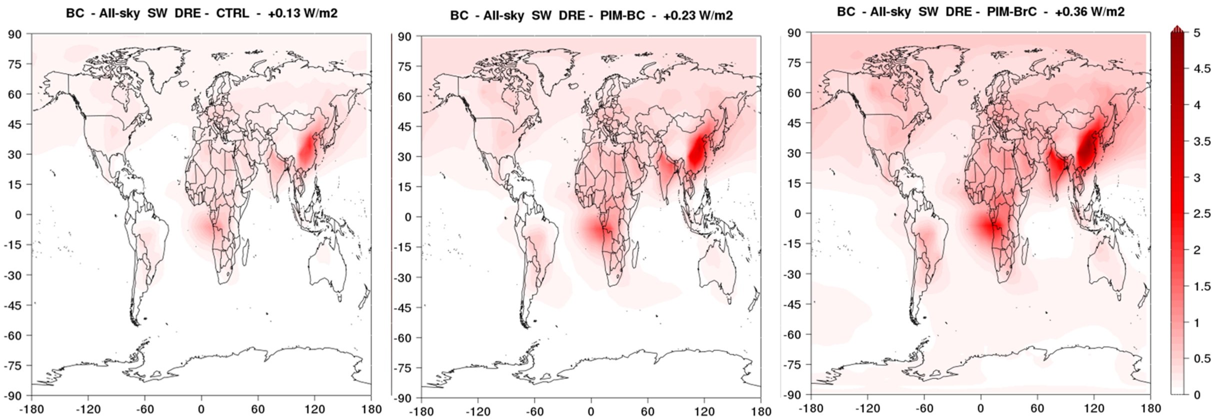

Figure 6. Annual mean (2010–2014) black carbon (BC) direct radiative effect (DRE) at top of the atmosphere calculated from CTRL, PIM-BC, and PIM-BrC experiments.

and other sources of BrC are aliphatic compounds (Laskin et al., 2015; Guang-Ming et al., 2016) and aqueous-phase chemical reactions in clouds. Moreover, we neglected the browning of some anthropogenic and biogenic SOA by reaction with ammonium (Bones et al., 2010; Updyke et al., 2012). Finally, another uncertainty in BrC absorption may arise from the fraction of POA emission that we assumed to be BrC. Jo et al. (2016) calculated the BrC emissions with a relationship between the modified combustion efficiency and AAE. According to their results, 45% and 17% of POA emitted by BF and BB sources, respectively, was BrC. Varying the emitted fractions by a factor 1.5, Jo et al. (2016) estimated an uncertainty of about 30% and 40% in primary BrC absorption for BF and BB sources, respectively. However, it should be noted that the inclusion of more BrC would increase the bias in AAE, because BrC is absorbing mainly at the wavelengths less than 550 nm.

Another factor that could affect our results is the coarse model resolution (4°×5°) used in this study. Specifically, previous studies (i.e., Rastigejev et al., 2010; Vignati et al., 2010) have shown that coarse-grid chemical and transport models do not calculate the right aerosol concentration because they are not able to reproduce the gradient of concentrations within a grid-box especially when the mixing with clean air occurs.

5. Implications for the DRE

5.1. DRE by Species

Figure 6 shows the TOA DRE of BC estimated from the simulations described in Table 3, and their global average values are reported in Table 7. The global average DRE values associated with BC were +0.13, +0.24, and +0.25 W/m^2 for CTRL, PIM-BC, and CS-BC simulations, respectively. According to our calculations, BC DRE thus increased by a factor of 1.8 with respect to CTRL when the full internal mixing is considered. DRE associated with CS-BC and PIM-BC differed by approximately 5%. The difference was not large because of the small burden of externally mixed (hydrophobic) BC, given the rapid ageing after its emission.

Table 7
Clear-sky and all-sky TOA DRE of BC (W/m^2)

Experiment	Clear Sky	All Sky
CTRL	+0.12	+0.13
PIM-BC	+0.21	+0.23
CS-BC	+0.22	+0.24
PIM-BrC	+0.34	+0.36
CS-BrC	+0.37	+0.39

Abbreviations: BC: black carbon; BrC: brown carbon; CS: core-shell; DRE: direct radiative effect; PIM: partial internal mixing; TOA: top of the atmosphere.

BC DRE obtained from CS-BC and PIM-BC was about 10% larger than that estimated by Wang et al. (2014) (+0.22 W/m^2) after that the same authors have scaled the AAOD to match the AERONET observations. Although in our work we have used the same treatment of Wang et al. (2014) for BC emission, ageing, and optical parameters, this difference was essentially due to two factors. First, Wang et al. (2014) did not use a CS model. E_{abs} associated with BC coating was considered by applying a constant absorption enhancement of 1.1 for FF and 1.5 for BF/BB BC. These values were lower than those of our E_{abs} (1.6–1.8) estimated at AERONET stations from our experiments with nonabsorbing OA.

Second, the BC lifetime (4.8 days) in our simulation was longer than that of Wang et al. (2014; 4.4 days). This difference is the result of the bias correction applied to the precipitation and is also likely due to the coarser grid used in our work (4°×5°) with respect to 2°×2.5° employed by Wang et al. (2014). At the same time, our BC lifetime is 1.7 times lower than the mean (8.2 days) of the values reported by Bond et al. (2013). This results in a lower DRE with respect to previous estimates. Our DRE calculated from the CTRL experiment was at the lower end of the interval of 0.1–0.57 W/m^2 (Saleh et al., 2015) estimated by model studies using the external mixing, while the DRE calculated in PIM-BC and CS-BC was approximately 1.5 times lower than the central value (0.38 W/m^2) obtained with models that consider internal mixing (Saleh et al., 2015). This finding is consistent with the results of Wang et al. (2014).

Considering the BrC, the BC DRE values were +0.37 and +0.40 W/m^2 for PIM-BrC and CS-BrC, respectively. The additional warming differs by approximately 8% compared with those for CS-BC and PIM-BC, respectively. BC DRE calculated by observational constraints on retrieved AAOD was +0.88 W/m^2 (0.17–1.48 W/m^2; Bond et al., 2013), and it was generally underestimated by chemical and transport models. Saleh et al. (2015) showed that the combination of the lensing effect and BrC absorption resolves the discrepancy existing between models (+0.30 and +0.38 W/m^2, for external and internal mixed BC, respectively) and observationally constrained prediction (+0.88 W/m^2). They estimated a DRE change of +0.51 W/m^2 with respect to a reference case with externally mixed BC and nonabsorbing OA. According to our model, we estimate a DRE change of +0.24 and +0.27 W/m^2 for PIM-BrC and CS-BrC, respectively. These values are halved with respect to the work of Saleh et al. (2015). The difference is mainly due to the blanching of BB BrC that Saleh et al. (2015) did not consider. Indeed, excluding the whitening of BB OA, our calculations produced a DRE change of +0.46 W/m^2, a value close to +0.51 W/m^2 reported by Saleh et al. (2015). The remaining difference (+0.05 W/m2) could be explained in terms of the different treatments used for BC ageing and size distribution. Other differences could be found in the model and optical properties treatment used for coating aerosols.

As discussed in sections 4 and 5, AAE was overestimated by 23% and 114% in PIM-BC and PIM-BrC experiments, respectively. Therefore, it is interesting to explore how this uncertainty could affect the estimation of DREs. The uncertainty was estimated through a correction of the modeled absorption spectral dependence with the observed AAE. The method used is reported in the supplements. According to our calculation, the uncertainties in PIM-BC and PIM-BrC DRE associated to AAE overestimation were 5–10% and 20–30%, respectively. This means that the PIM-BrC DRE resulting from a correct representation of AAE was likely within the range of 0.44–0.49 W/m^2, implying a DRE change (with respect to CTRL) of 0.31–0.36 W/m^2. In other words, the underestimation of DRE change was 23–33%. Uncertainty associated with BrC treatment was in the range of −36%/+66%. It was estimated by assuming no BrC absorption (PIM-BC simulation), no blanching of BrC emitted from BB sources, and an increase of BrC absorption of 40%, due to the increasing of a factor 1.5, related to the fraction emitted as primary absorbing OA (see section 4; Jo et al., 2016).

Figure 7 shows the SW, LW, and total (SW+LW) TOA DRE exerted by the dust particles, and their global average values are reported in Table 8. The spatial pattern of SW dust DRE shows a dependence on the dust particle dimensions and surface albedo. Regarding SW, a warming effect dominates close to the sources, given the abundance of larger particles and presence of a high reflecting surface. By contrast, far from source regions, where the dust population is dominated by finer particles, DRE is negative, especially above the dark surfaces of the oceans. Middle (DUST-M) and high (DUST-H) dust absorption experiments exhibit a lower cooling effect far from the sources and a larger warming effect above the desert with respect to the DUST-L experiment. The global average dust SW DRE values were −0.18, +0.02, and +0.13 W/m^2 for DUST-L, DUST-M, and DUST-H, respectively.

Considering the nonspherical shape, dust SW DRE is less warming above the desert and more cooling far from the sources, with a global average value of −0.22 W/m^2 (DUST-NS). This value is 22% less than that obtained in the reference case (DUST-L). Assuming that the perturbation induced by nonspherical particles is equal to the difference between DUST-NS and DUST-L, the SW DRE for DUST-M and DUST-H decreased to +0.01 and +0.10 W/m^2, respectively.

Dust LW DRE was positive everywhere, especially close to the sources, where DRE was larger than +2 W/m^2. The global average dust LW DRE was similar for all the experiments, being +0.08 W/m^2 in

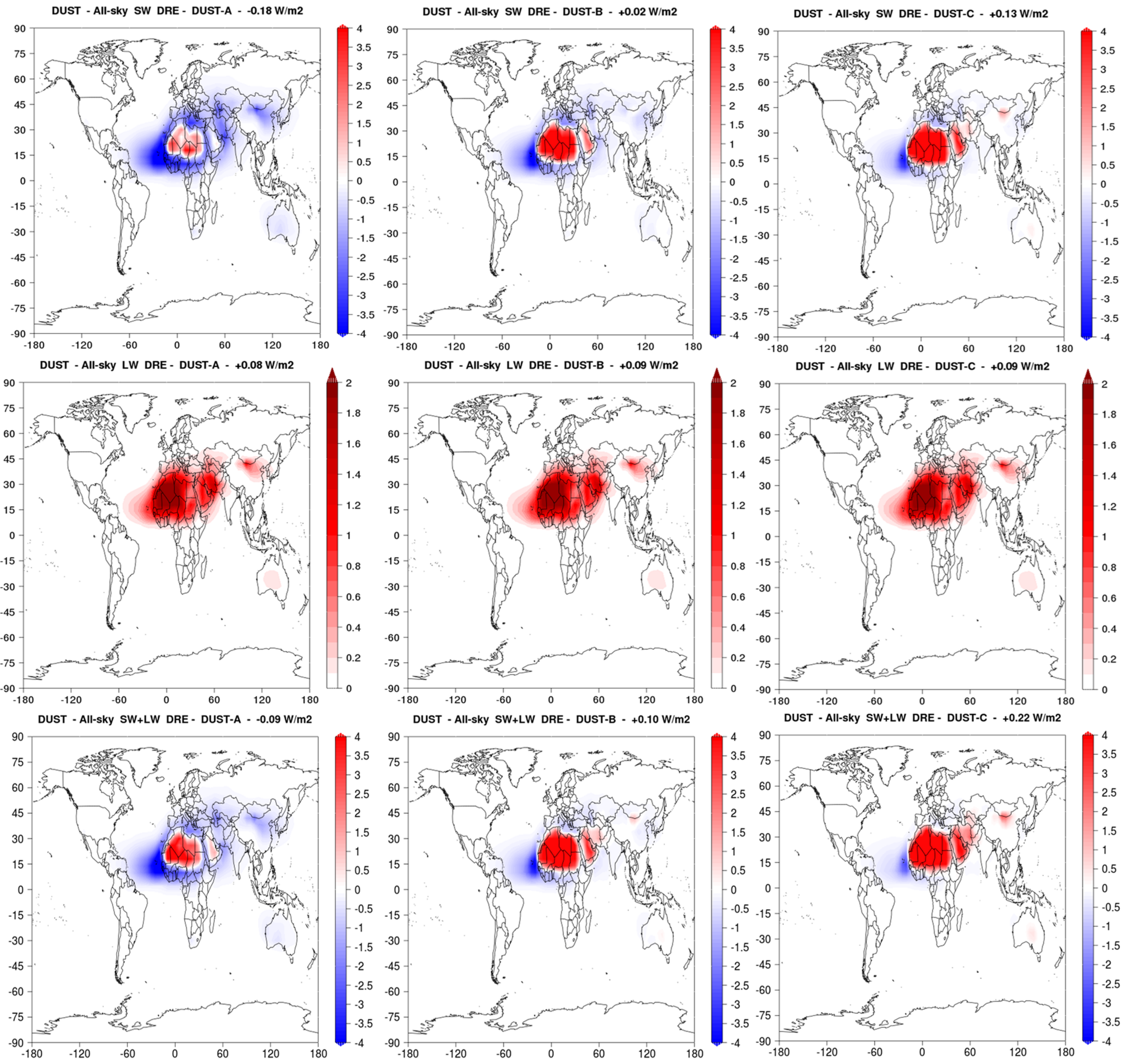

Figure 7. Shortwave (SW), longwave (LW), and net annual mean (2010–2014) dust direct radiative effect (DRE) at top of the atmospherecalculated from DUST-L, DUST-M, and DUST-H simulations.

Table 8
SW, LW, and total TOA DRE of dust (W/m^2)

Experiment	SW	LW	SW+LW
DUST-L	−0.26	+0.12	−0.14
DUST-M	−0.05	+0.12	+0.07
DUST-H	+0.08	+0.12	+0.20
DUST-NS	−0.31	+0.12	−0.19
DUST-L	−0.18	+0.08	−0.10
DUST-M	+0.02	+0.09	+0.11
DUST-H	+0.13	+0.09	+0.22
DUST-NS	−0.22	+0.08	−0.14

Abbreviations: DRE: direct radiative effect; LW: longwave; SW: shortwave; TOA: top of the atmosphere.

DUST-L and +0.09 W/m^2 in DUST-M and DUST-H simulations. The impact of the nonspherical shape on the LW radiation has not been investigated because it is expected to be negligible with respect to SW (Pitari et al., 2015).

The total dust DRE values were −0.10, +0.11, and +0.22 W/m^2 for DUST-L, DUST-M, and DUST-H experiments, respectively. Considering the nonspherical shape, the total DRE values were −0.13, +0.10, and +0.19 W/m^2, respectively, for the same experiments. These values were within the range (from −0.48 to +0.20 W/m^2) estimated by Kok et al. (2017) from an ensemble of models constrained by the observations of aerosol abundance, and they were also comparable to the results reported by Scanza et al. (2015), which used a dust size distribution based on Kok (2011). Although our dust DRE estimations were within the range reported in the most recent findings, we noticed that the absolute difference of dust DRE between high and low absorbing simulation was 0.32 W/m^2, highlighting the uncertainties related to the imaginary part of the dust refractive index. Finally, we also point out that the uncertainty related to the dust particle shape was smaller (up to 0.03 W/m^2) with respect to the one associated to the refractive index.

5.2. Total DRE

Global average AAOD and DRE by all RAAs has been estimated using as central value the combination of PIM-BrC and DUST-M simulation and taking into account the nonspherical shape of soil dust particles. According to our model, total AAOD (at 550 nm) was 0.0050 (0.0030 for BC-BrC mixture and 0.0020 for dust) with an all-sky DRE of +0.46 W/m^2. We estimated an overall uncertainty for total DRE related to mixing state, BrC treatment, and dust optical properties of −57%/+59% (0.20–0.73 W/m^2). The uncertainties associated to model assumptions were deduced comparing the various simulation against the central value. Total uncertainty was calculated as the root sum of single squared errors, assuming that the uncertainties discussed below are independent.

The uncertainty related to the mixing state was −30%/+7%. It was calculated comparing the central value against EXT-BrC and CS-BrC simulations combined with DUST-M (with nonspherical particles). The uncertainty due to AAE overestimation was +20%. Since the latter is most likely due to the use of CS (section 4), it may be incorporated within the uncertainties associated to mixing state assumption.

Total DRE decreases by 22% not accounting for BrC absorption and increases by 41% if we do not consider the blanching of BB-BrC. As discussed in section 4, according to Jo et al. (2016), increasing by a factor 1.5, the fraction emitted as primary absorbing OA produces an increase up to 40% of BrC absorption. This results roughly in a change of total DRE by +28%.

The uncertainty associated to dust refractive index was −43%/+20%. It has been estimated comparing the central value against PIM-BrC combined with DUST-L and DUST-H (both with nonspherical particles), respectively. Finally, the uncertainty due to dust shape has been calculated to be up to +14%.

According to the values reported above, the lower bound of uncertainties in RAAs DRE is dominated by dust refractive indices, instead the upper bound by BrC treatment. We highlight that other uncertainties, which were not investigated in our study, could affect the total DRE by RAAs. One of these is the vertical distribution of BC, which contributes at least 20% of the present uncertainty in modeled BC DRE (Samset et al., 2013), but may reaches also 35–40% (Zarzycki & Bond, 2010; Wang et al., 2014). Dust vertical distribution is also important for DRE, especially for LW forcing (Liao & Seinfeld, 1998; Shell & Somerville, 2007). Aerosol radiative effect is also sensitive to clouds and surface albedo. As shown by Ocko et al. (2012), increasing of cloud cover strengthens BC forcing and reduces the DRE by organic compounds. The effect of surface albedo on RAA DRE is large in areas with persistent reflective surfaces (as Sahara and Arctic; Myhre et al., 2013) and could depend on the assumptions done for albedo parameterization, especially for snow and ice (Schulz et al., 2006).

6. Conclusions

In the present work, we studied the sensitivity of the absorption properties of carbonaceous aerosol to the mixing state hypothesis, absorption of OA (BrC), and sensitivity of dust particle absorption to its refractive index and shape. We have also investigated the implications for DRE. The RAA mass concentrations (BC, BrC, and dust) and their optical properties have been simulated to include the most recent updates in terms of ageing, size distribution, and absorption properties inferred from observational constraints.

At AERONET stations dominated by carbonaceous aerosol absorption, simulated AAOD at 440 nm was well correlated with the observations, but the better agreement between the model and observations was obtained by including BrC absorption in the optical calculations (CS-BrC and PIM-BrC). The AAOD obtained with PIM* simulations is approximately 10% less than that calculated in the CS* experiments. BC absorption enhancement calculation has shown that E_{abs} at 440 is in the range of 1.7–1.9

for the simulations including a nonabsorbing coating. By contrast, including the BrC absorption, E_{abs} is in the range of 2.8–3.4.

The sensitivity of dust particle absorption has been investigated using three different refractive index databases that we classify as low (DUST-L), middle (DUST-M), and high (DUST-H) absorption. At AERONET stations dominated by dust absorption, the modeled AAOD correlation was larger than 0.80 and bias values were −14%, +6.1%, and +23% for low, middle, and high dust absorption scenarios, respectively. The results suggest that the spherical assumption does not play an important role in the total uncertainty in simulating AAOD.

SSA was overestimated by approximately +5.5% in the CTRL case. When aerosol particles are considered internally mixed, the model bias decreased to +3.3% and +3.7% in CS-BC and PIM-BC, respectively. When the BC was coated or partially coated by absorbing OA, the bias was lowered to −0.55% and −0.45%. Increasing the dust particle absorption, SSA was underestimated by −0.35% and −1.0% in DUST-M and DUST-H, respectively. Considering the nonspherical shape of dust particles (DUST-NS), the SSA bias was decreased by approximately 22% with respect to the spherical particle case (DUST-L). Additional analysis showed that uncertainty in SSA measurements likely affected the comparison between modeled and observed SSA. Model scores increased removing from the observations the SSA values with larger uncertainty.

The observed average AAE (between 440 and 675) was overestimated in the model especially in the simulation including the BrC. This indicated that modeled absorption decreased more rapidly with the wavelength reflecting a larger influence of BrC and dust most likely due to the use of Mie theory to calculate the freshly emitted and coated BC optical properties.

The DRE TOA values of BC calculated from our experiments were +0.13, +0.24, and +0.25 W/m^2 for CTRL, PIM-BC, and CS-BC simulations, respectively. The BC DRE values calculated including the absorption of BrC were +0.37 and +0.40 W/m^2 for PIM-BrC and CS-BrC, respectively. Saleh et al. (2015) have shown that including the BrC coating on the BC, the DRE changed of +0.51 W/m^2 with respect to a reference case with externally mixed BC and not absorbing OA. By contrast, we have estimated a reduced DRE change (+0.27 W/m^2) compared with that of Saleh et al. (2015). Our results suggested that the absorption enhancement of BC due to BrC coating has been overestimated previously. The overestimation is mainly due to the blanching of BB BrC that Saleh et al. (2015) did not consider in their study. Further analysis showed that the uncertainty in PIM-BrC due to AAE overestimation was 20–30%, implying an underestimation of DRE change by 23–33%, while the uncertainties associated to BrC treatment were in the range −36%/+66%.

The SW DRE values of dust were −0.18, +0.02, and +0.13 W/m^2 for low, middle, and high absorption cases, respectively. The nonspherical shape reduces these values by 22% (−0.04 W/m^2). The LW DRE of dust was estimated to be approximately 0.08 W/m^2 and did not exhibit a particular sensitivity to the refractive index. The total dust DRE values were −0.10, +0.11, and +0.22 W/m^2, for DUST-L, DUST-M, and DUST-H experiments, respectively. Introducing the nonspherical shape, the dust DRE values were −0.13, +0.10, and +0.19 W/m^2 for low, middle, and high dust absorption experiments, respectively.

According to our results, soil dust DRE is more sensitive to the complex part of the refractive index than to shape assumption. The spread between the DRE associated with DUST-L and DUST-H (+0.32 W/m^2) reflects the uncertainties in the modeling of climatic effects of dust particles associated with its mineral composition. These results suggest that further studies are required to understand and reduce the uncertainties of dust optical properties.

Global average all-sky DRE by all RAAs was +0.46 W/m^2. Uncertainties in aerosol mixing state, BrC treatment, and soil dust optical properties suggested an overall uncertainty in total DRE of −57%/+59% (0.20–0.73 W/m^2). According to our models, total uncertainty RAAs DRE was mainly related to soil dust refractive index and brown carbon treatment.

Competing interests

The authors declare that they have no conflicts of interest.

AppendixA: List of acronyms and statistical indices.

Table A1
List of Acronyms and Symbols

Acronym	Definition
AAE	Absorption Ångström exponent
AAOD	Absorbing aerosol optical depth
AERONET	Aerosol robotic network
AOD	Aerosol optical depth
BB	Biomass burning
BC	Black carbon
BF	Bio fuel
BrC	Brown carbon
CCN	Cloud condensation nuclei
CS	Core shell
DEAD	Dust Entrainment And Deposition
DRE	Direct radiative effect
DRF	Direct radiative forcing
E_{abs}	Black carbon absorption enhancement factor
FF	Fossil fuel
FlexAOD	Flexible aerosol optical depth
IN	Ice nuclei
MAC	Mass absorption coefficient
MERRA2	Modern Era Retrospective-analysis for Research and Application version 2
OA	Organic aerosol
PIM	Partial internal mixing
POA	Primary organic aerosol
RAA	Radiation-absorbing aerosol
RF	Radiative forcing
RRTMG	Rapid radiative transfer model for GCM
SAOD	Scattering aerosol optical depth
SOA	Secondary organic aerosol
SSA	Single-scattering albedo

Table A2
Definition of the Statistical Indices Used in the Analysis

Index	Definition
n	Number of available data
O_i	ith observation
M_i	ith modeled value, paired with O_i
$\overline{O}$	Mean observed value $\frac{1}{n}\sum_i^n O_i$
$\overline{M}$	Mean modeled value $\frac{1}{n}\sum_i^n M_i$
FAC2	fraction of modeled values within a factor of 2 of observations $\frac{1}{n}\sum_i^n i:\left(0.5<\frac{M_i}{O_i}<2\right)$
MB	Mean bias $\frac{1}{n}\sum_i^n (M_i - O_i)$
NMB	Mean normalized bias $\frac{1}{n}\sum_i^n \frac{(M_i - O_i)}{O_i}$
r	Pearson correlation coefficient $\frac{1}{n-1}\sum_i^n \frac{(O_i-\overline{O})}{\sigma_O}\frac{(M_i-\overline{M})}{\sigma_M}$

Acknowledgments
AcknowledgementsPaolo Tuccella is beneficiary of an AXA Research Fund postdoctoral grant. Seungun Lee was supported by the National Research Foundation of Korea (NRF) grant funded by the Korean government (MSIT) (2018004494). The authors are grateful to Xuan Wang for the precious and profitable suggestions about the simulation of brown carbon with GEOS-Chem. We thank the GEOS-Chem developers for making the model available to the scientific community. We thank also NASA for making freely available the AERONET measurements and T-MATRIX code. Finally, the authors are grateful to four anonymous reviewers for their suggestions and constructive comments that helped to significantly improve this paper. Data availability: Users can access the GEOS-Chem simulations used in this study at this link: https://osf.io/xntr8/. AERONET data are freely available at the following website https://aeronet.gsfc.nasa.gov/new_web/data.html. FlexAOD postprocessing tool can be provided upon request to gabriele.curci@aquila.infn.it. T-MATRIX code may be downloaded at this link https://www.giss.nasa.gov/staff/mmishchenko/t_matrix.html.

References

Alexander, B., Park, R. J., Jacob, D. J., Li, Q. B., Yantosca, R. M., Savarino, J., et al. (2005). Sulfate formation in sea-salt aerosols: Constraints from oxygen isotopes. *Journal of Geophysical Research*, *110*, D10307. https://doi.org/10.1029/2004JD005659

Alexander, D. T. L., Crozier, P. A., & Anderson, J. R. (2008). Brown carbon spheres in East Asian outflow and their optical properties. *Science*, *321*(5890), 833–836. https://doi.org/10.1126/science.1155296

Andreae, M. O., & Gelencsér, A. (2006). Black carbon or brown carbon? The nature of light-absorbing carbonaceous aerosols. *Atmospheric Chemistry and Physics*, *6*, 3131–3148. https://doi.org/10.5194/acp-6-3131-2006

Andreae, M. O., & Rosenfeld, D. (2008). Aerosol-cloud-precipitation interactions. Part 1. The nature and sources of cloud-active aerosols. *Earth-Science Reviews*, *89*, 13–41. https://doi.org/10.1016/j.earscirev.2008.03.001

Arola, A., Schuster, G., Myhre, G., Kazadzis, S., Dey, S., & Tripathi, S. N. (2011). Inferring absorbing organic carbon content from AERONET data. *Atmospheric Chemistry and Physics*, *11*, 215–225. https://doi.org/10.5194/acp-11-215-2011

Bahadur, R., Praveen, P. S., Xu, Y., & Ramanathan, V. (2012). Solar absorption by elemental and brown carbon determined from spectral observations. *Proceedings of the National Academy of Sciences of the USA*, *109*, 17366–17371.

Bey, I., Jacob, D. J., Yantosca, R. M., Logan, J. A., Field, B., Fiore, A. M., et al. (2001). Global modeling of tropospheric chemistry with assimilated meteorology: Model description and evaluation. *Journal of Geophysical Research*, *106*, 23073–23095.

Bond, T. C., & Bergstrom, R. W. (2006). Light absorption by carbonaceous particles: An investigative review. *Aerosol Science and Technology*, *40*, 27–67. https://doi.org/10.1080/02786820500421521

Bond, T. C., E. Bhardwaj, R. Dong, R., Jogani, S. K. Jung, C. Roden, D. G. Streets, and N. M. Trautmann (2007), Historical emissions of black and organic carbon aerosol from energy-related combustion, 1850–2000, *Global Biogeochem. Cy.*, *21*, GB2018, doi:https://doi.org/10.1029/2006GB002840.

Bond, T. C., Doherty, S., Fahey, D., Forster, P., Berntsen, T., DeAngelo, B., et al. (2013). Bounding the role of black carbon in the climate system: A scientific assessment. *Journal of Geophysical Research-Atmospheres*, *118*, 5380–5552. https://doi.org/10.1002/jgrd.50171

Bond, T. C., Habib, G., & Bergstrom, R. W. (2006). Limitations in the enhancement of visible light absorption due to mixing state. *Journal of Geophysical Research-Atmospheres*, *111*. https://doi.org/10.1029/2006JD007315

Bones, D. L., Henricksen, D. K., Mang, S. A., Gonsior, M., Bateman, A. P., Nguyen, T. B., et al. (2010). Appearance of strong absorbers and fluorophores in limonene-O3 secondary organic aerosol due to NH4+-mediated chemical aging over long time scales. *Journal of Geophysical Research*, *115*, D05203. https://doi.org/10.1029/2009JD012864

Boucher, O., Randall, D., Artaxo, P., Bretherton, C., Feingold, G., Forster, P., et al. (2013). Clouds and aerosols. In T. F. Stocker, D. Qin, G.-K. Plattner, M. Tignor, S. K. Allen, J. Boschung, A. Nauels, Y. Xia, V. Bex, & P. M. Midgley (Eds.), *Climate change 2013: The physical science basis. Contribution of Working Group I to the Fifth Assessment Report of the Intergovernmental Panel on Climate Change* (Chap. 7, pp. 571–568). Cambridge, United Kingdom and New York, NY, USA: Cambridge University Press.

Chen, Y., & Bond, T. C. (2010). Light absorption by organic carbon from wood combustion. *Atmospheric Chemistry and Physics*, *10*, 1773–1787. https://doi.org/10.5194/acp-10-1773-2010

Cheng, Y., He, K. B., Engling, G., Weber, R., Liu, J. M., Du, Z. Y., & Dong, S. P. (2017). Brown and black carbon in Beijing aerosol: Implications for the effects of brown coating on light absorption by black carbon. *Science of the Total Environment*, *599*, 1047–1055. 5//WOS:000405253500001

Cheng, Y. F., Eichler, H., Wiedensohler, A., Heintzenberg, J., Zhang, Y. H., Hu, M., et al. (2006). Mixing state of elemental carbon and non-light-absorbing aerosol components derived from in situ particle optical properties at Xinken in Pearl River Delta of China. *Journal of Geophysical Research*, *111*(D20), D20204. https://doi.org/10.1029/2005JD006929

Cheng, Y. F., Su, H., Rose, D., Gunthe, S. S., Berghof, M., Wehner, B., et al. (2012). Size-resolved measurement of the mixing state of soot in the megacity Beijing, China: Diurnal cycle, aging and parameterization. *Atmospheric Chemistry and Physics*, *12*(10), 4477–4491. https://doi.org/10.5194/acp-12-4477-2012

Chin, M., Chu, A., Levy, R., Remer, L., Kaufman, Y., Holben, B., et al. (2004). Aerosol distribution in the Northern Hemisphere during ACE-Asia: Results from global model, satellite observations, and Sunphotometer measurements. *Journal of Geophysical Research*, *109*, D23S90. https://doi.org/10.1029/2004JD004829

China, S., Mazzoleni, C., Gorkowski, K., Aiken, A. C., & Dubey, M. K. (2013). Morphology and mixing state of individual freshly emitted wildfire carbonaceous particles. *Nature Communications*, *4*, 2122. https://doi.org/10.1038/ncomms3122

China, S., Scarnato, B., Owen, R. C., Zhang, B., Ampadu, M. T., Kumar, S., et al. (2015). Morphology and mixing state of aged soot particles at a remote marine free troposphere site: Implications for optical properties. *Geophysical Research Letters*, *42*(4), 1243–1250. https://doi.org/10.1002/2014GL062404

Choobari, O. A., Zawar-Reza, P., & Sturman, A. (2013). The global distribution of mineral dust and its impact on the climate system: A review. *Atmospheric Research*, *138*, 152–165. https://doi.org/10.1016/j.atmosres.2013.11.007

Curci, G., Alyuz, U., Barò, R., Bianconi, R., Bieser, J., Christensen, J. H., et al. (2019). Modelling black carbon absorption of solar radiation: Combining external and internal mixing assumptions. *Atmospheric Chemistry and Physics*, *19*(1), 181–204. https://doi.org/10.5194/acp-19-181-2019

Curci, G., Hogrefe, C., Bianconi, R., Im, U., Balzarini, A., Baró, R., et al. (2015). Uncertainties of simulated aerosol optical properties induced by assumptions on aerosol physical and chemical properties: An AQMEII-2 perspective. *Atmospheric Environment*, *115*, 541–552. https://doi.org/10.1016/j.atmosenv.2014.09.009

Dubovik, O., Holben, B., Eck, T. F., Smirnov, A., Kaufman, Y. J., King, M. D., et al. (2002). Variability of absorption and optical properties of key aerosol types observed in worldwide locations. *Journal of the Atmospheric Sciences*, *59*, 590–608.

Feng, Y., Ramanathan, V., & Kotamarthi, V. R. (2013). Brown carbon: A significant atmospheric absorber of solar radiation? *Atmospheric Chemistry and Physics*, *13*, 8607–8621. https://doi.org/10.5194/acp-13-8607-2013

Formenti, P., Schütz, L., Balkanski, Y., Desboeufs, K., Ebert, M., Kandler, K., et al. (2011). Recent progress in understanding physical and chemical properties of African and Asian mineral dust. *Atmospheric Chemistry and Physics*, *11*(16), 8231–8256. https://doi.org/10.5194/acp-11-8231-2011

Forrister, H., Liu, J., Scheuer, E., Dibb, J., Ziemba, L., Thornhill, K. L., et al. (2015). Evolution of brown carbon in wildfire plumes. *Geophysical Research Letters*, *42*(11), 4623–4630. https://doi.org/10.1002/2015GL063897

Gilgio, L., Randerson, J. T., & van der Werf, G. R. (2013). Analysis of daily, monthly, and annual burned area using the fourth generation global fire emissions database (GFED4). *Journal of Geophysical Research*, *118*, 317–328.

Ginoux, P., Chin, M., Tegen, I., Prospero, J. M., Holben, B., Dubovik, O., & Lin, S.-J. (2001). Sources and distribution of dust aerosols simulated with the GOCART model. *Journal of Geophysical Research*, *106*(20255-2027), 2001. https://doi.org/10.1029/2000JD000053

Ginoux, P., Prospero, J. M., Gill, T. E., Hsu, N. C., & Zao, M. (2012). Global-scale attribution of anthropogenic and natural dust sources and their emission rates based on MODIS deep blue aerosol products. *Reviews of Geophysics*, *50*, RG3005. https://doi.org/10.1029/2012RG000388

Guang-Ming, W., Zhi-Yuan, C., Shi-Chang, K., Kawamura, K., Ping-Qing, F., Yu-Lan, Z., et al. (2016). Brown carbon in the cryosphere: Current knowledge and perspective. *Advances in Climate Change Research*, *7*, 82–89.

Guenther, A., Karl, T., Harley, P., Wiedinmyer, C., Palmer, P. I., & Geron, C. (2006). Estimates of global terrestrial isoprene emissions using MEGAN (Model of Emissions of Gases and Aerosols from Nature). *Atmospheric Chemistry and Physics*, *6*, 3181–3210.

Gustafsson, O., & Ramanathan, V. (2016). Convergence on climate warming by black carbon aerosols. *Proceedings of the National Academy of Sciences of the USA*, *113*, 4243–4245.

Hansen, J., Sato, M., & Ruedy, R. (1997). Radiative forcing and climate response. *Journal of Geophysical Research*, *102*, 6831–6894. https://doi.org/10.1029/96JD03436

Haywood, J., & Boucher, O. (2000). Estimates of the direct and indirect aerosol radiative forcing due to tropospheric aerosols: A review. *Reviews of Geophysics*, *38*, 513–543. https://doi.org/10.1029/1999RG000078

He, C., Liou, K.-N., Takano, Y., Zhang, R., Levy Zamora, M., Yang, P., et al. (2015). Variation of the radiative properties during black carbon aging: Theoretical and experimental intercomparison. *Atmospheric Chemistry and Physics*, *15*, 11967–11980. https://doi.org/10.5194/acp-15-11967-2015

Heald, C. L., Ridley, D. A., Kroll, J. H., Barrett, S. R. H., Cady-Pereira, K. E., Alvarado, M.- J., & C. D. (2014). Contrasting the direct radiative effect and direct radiative forcing of aerosols. *Atmospheric Chemistry and Physics*, *14*, 5513–5527. https://doi.org/10.5194/acp-14-5513-2014

Hecobian, A., Zhang, X., Zheng, M., Frank, N., Edgerton, E. S., & Weber, R. J. (2010). Water-Soluble Organic Aerosol material and the light-absorption characteristics of aqueous extracts measured over the Southeastern United States. *Atmospheric Chemistry and Physics*, *10*, 5965–5977. https://doi.org/10.5194/acp-10-5965-2010

Hess, M., Koepke, P., & Schult, I. (1998). Optical properties of aerosols and clouds: The software package OPAC. *Bulletin of the American Meteorological Society*, *79*, 831e844.

Holben, B. N., Tanré, D., Smirnov, A., Eck, T. F., Slutsker, I., Abuhassan, N., et al. (2001). An emerging ground-based aerosol climatology: Aerosol Optical Depth from AERONET. *Journal of Geophysical Research*, *106*(D11), 12067–12097. https://doi.org/10.1029/2001JD900014

Huneeus, N., et al. (2011). Global dust model intercomparison in AeroCom phase I. *Atmospheric Chemistry and Physics*, *11*, 7781–7816. https://doi.org/10.5194/acp-11-7781-2011

Iacono, M. J., Delamere, J. S., Mlawer, E. J., Shephard, M. W., Clough, S. A., & Collins, W. D. (2008). Radiative forcing by long-lived greenhouse gases: Calculations with the AER radiative transfer models. *Journal of Geophysical Research*, *113*, D13103. https://doi.org/10.1029/2008JD009944

Jacobson, M. Z. (2000). A physically-based treatment of elemental carbon optics: Implications for global direct forcing of aerosols. *Geophysical Research Letters*, *27*, 217–220. https://doi.org/10.1029/1999GL010968

Jacobson, M. Z. (2001). Global direct radiative forcing due to multicomponent anthropogenic and natural aerosols. *Journal of Geophysical Research*, *106*, 1551–1568.

Jaeglé, L., Quinn, P. K., Bates, T. S., Alexander, B., & Lin, J.-T. (2011). Global distribution of sea salt aerosols: New constraints from in situ and remote sensing observations. *Atmospheric Chemistry and Physics*, *11*, 3137–3157. https://doi.org/10.5194/acp-11-3137-2011

Jethva, H., Torres, O., & Ahn, C. (2014). Global assessment of OMI aerosol single- scattering albedo using ground- based AERONET inversion. *Journal of Geophysical Research-Atmospheres*, *119*(9020-9040), 2014.

Jin, X., Fiore, A. M., Curci, G., Lyapustin, A., Civerolo, K., Ku, M., et al. (2019). Assessing uncertainties of a geophysical approach to estimate surface fine particulate matter distributions from satellite-observed aerosol optical depth. *Atmospheric Chemistry and Physics*, *19*, 295–313. https://doi.org/10.5194/acp-19-295-2019

Jo, D. S., Park, R. J., Lee, S., Kim, S.-W., & Zhang, X. (2016). A global simulation of brown carbon: Implications for photochemistry and direct radiative effect. *Atmospheric Chemistry and Physics*, *16*, 3413–3432. https://doi.org/10.5194/acp-16-3413-2016

Johnson, M. S., Meskhidze, N., & Praju Kiliyanpilakkil, V. (2012). A global comparison of GEOS-Chem predicted and remotely-sensed mineral dust aerosol optical depth and extinction profiles. *Journal of Advances in Modeling Earth Systems*, *4*, M07001. https://doi.org/10.1029/2011MS000109

Khalizov, A. F., Xue, H. X., Wang, L., Zheng, J., & Zhang, R. Y. (2009). Enhanced light absorption and scattering by carbon soot aerosol internally mixed with sulfuric acid. *The Journal of Physical Chemistry*, *113*(6), 1066–1074. https://doi.org/10.1021/jp807531n

Kirchstetter, T. W., & Thatcher, T. L. (2012). Contribution of organic carbon to wood smoke particulate matter absorption of solar radiation. *Atmospheric Chemistry and Physics*, *12*, 6067–6072. https://doi.org/10.5194/acp-12-6067-2012

Kok, J. F. (2011). A scaling theory for the size distribution of emitted dust aerosols suggests climate models underestimate the size of the global dust cycle. *PNAS*, *108*(3), 1016–1021. https://doi.org/10.1073/pnas.1014798108

Kok, J. F., Ridley, D. A., Zhou, Q., Miller, R. L., Zhao, C., Colette, L. H., et al. (2017). Smaller desert dust cooling effect estimated from analysis of dust size and abundance. *Nature Geoscience*, *10*(4), 274–278. https://doi.org/10.1038/NGEO2912

Lambe, A. T., Cappa, C. D., Massoli, P., Onasch, T. B., Forestieri, S. D., Martin, A. T., et al. (2013). Relationship between oxidation level and optical properties of secondary organic aerosol. *Environmental Science & Technology*, *47*(12), 6349–6357. https://doi.org/10.1021/es401043j

Laskin, A., Laskin, J., & Nizkorodov, S. A. (2015). Chemistry of atmospheric brown carbon. *Chemical Reviews*, *115*(4335–4382), 2015.

Lesins, G., Chylek, P., & Lohmann, U. (2002). A study of internal and external mixing scenarios and its effect on aerosol optical properties and direct radiative forcing. *Journal of Geophysical Research*, *107*(D10). https://doi.org/10.1029/2001JD000973

Liao, H., & Seinfeld, J. H. (1998). Radiative forcing by mineral dust aerosols: sensitivity to key variables. *Journal of Geophysical Research*, *103*, 31637–31645.

Lin, G., Penner, J. E., Flanner, M., Sillman, S., Xu, L., & Zhou, C. (2014). Radiative forcing of organic aerosol in the atmosphere and on snow: Effects of SOA and brown carbon. *Journal of Geophysical Research-Atmospheres*, *119*, 7453–7476. https://doi.org/10.1002/2013JD021186

Liu, C., Chung, C. E., Yin, Y., & Schnaiter, M. (2018). The absorption Ångström exponent of black carbon: From numerical aspects. *Atmospheric Chemistry and Physics*, *18*, 6259–6273. https://doi.org/10.5194/acp-18-6259-2018

Liu, D., Whitehead, J., Alfarra, M. R., Reyes-Villegas, E., Spracklen, D. V., Reddington, C. L., et al. (2017). Black-carbon absorption enhancement in the atmosphere determined by particle mixing state. *Nature Geoscience*, *10*(3), 184–188. https://doi.org/10.1038/ngeo2901

Liu, H. Y., Jacob, D. J., Bey, I., & Yantosca, R. M. (2001). Constraints from Pb-210 and Be-7 on wet deposition and transport in a global three-dimensional chemical tracer model driven by assimilated meteorological fields. *Journal of Geophysical Research-Atmospheres*, *106*, 12109–12128.

Liu, J., Fan, S., Horowitz, L. W., & Levy, H. II (2011). Evaluation of factors controlling long-range transport of black carbon to the Arctic. *Journal of Geophysical Research*, *116*, D04307. https://doi.org/10.1029/2010JD015145

Lukács, H., Gelencsér, A., Hammer, S., Puxbaum, H., Pio, C., Legrand, M., et al. (2007). Seasonal trends and possible sources of brown carbon based on 2-year aerosol measurements at six sites in Europe. *Journal of Geophysical Research*, *112*, D23S18. https://doi.org/10.1029/2006JD008151

Luo, J., Zhang, Y., Wang, F., & Zhang, Q. (2018). Effects of brown coatings on the absorption enhancement of black carbon: A numerical investigation. *Atmospheric Chemistry and Physics*, *18*, 16897–16914. https://doi.org/10.5194/acp-18-16897-2018

Mie, G. (1908). Beiträge zur Optik trüber Medien, speziell kolloidaler Metallösungen. *Ann. Phys.*, *330*, 377–445.

Mishchenko, M. I., Dlugach, J. M., Yanovitskij, E. G., & Zakharova, N. T. (1999). Bidirectional reflectance of flat, optically thick particulate layers: An efficient radiative transfer solution and applications to snow and soil surfaces. *Journal of Quantitative Spectroscopy & Radiative Transfer*, *63*(2–6), 409–432. https://doi.org/10.1016/S0022-4073(99)00028-X

Mishchenko, M. I., & Travis, L. D. (1998). Capabilities and limitations of a current fortran implementation of the T-matrix method for randomly oriented, rotationally symmetric scatterers. *Journal of Quantitative Spectroscopy & Radiative Transfer*, *60*(3), 309D324.

Mishchenko, M. I., Travis, L. D., & Mackowski, D. W. (1996). T-matrix computations of light scattering by nonspherical particles: A review. *Journal of Quantitative Spectroscopy & Radiative Transfer*, *55*, 535–575.

Myhre, G., Samset, B. H., Schulz, M., Balkanski, Y., Bauer, S., Berntsen, T. K., et al. (2013). Radiative forcing of the direct aerosol effect from AeroCom Phase II simulations. *Atmospheric Chemistry and Physics*, *13*(4), 1853–1877. https://doi.org/10.5194/acp-13-1853-2013

Ocko, I. B., Ramaswamy, V., Ginoux, P., Ming, Y., & Horowitz, L. W. (2012). Sensitivity of scattering and absorbing aerosol direct radiative forcing to physical climate factors. *Journal of Geophysical Research*, *117*, D20203. https://doi.org/10.1029/2012JD018019

Olivier, J. G. J., & Berdowski, J. J. M. (2001). Global emissions sources and sinks. In J. Berdowski, R. Guicherit, & B. J. Heij (Eds.), *The climate system*, (pp. 33–78). Lisse, Netherlands: A. A. Balkema Publ./Swets & Zeitlinger Publ.

Park, R. J., Jacob, D. J., Chin, M., & Martin, R. V. (2003). Sources of carbonaceous aerosols over the United States and implications for natural visibility. *Journal of Geophysical Research*, *108*, 4355. https://doi.org/10.1029/2002JD003190

Park, R. J., Jacob, D. J., Field, B. D., Yantosca, R. M., & Chin, M. (2004). Natural and transboundary pollution influences on sulfate-nitrate-ammonium aerosols in the United States: Implications for policy. *Journal of Geophysical Research*, *109*, D15204.

Park, R. J., Kim, M. J., Jeong, J. I, Youn, D., & Kim, S. (2010). A contribution of brown carbon aerosol to the aerosol light absorption and its radiative forcing in East Asia. *Atmospheric Environment*, *44*, 1414–1421.

Petzold, A., Rasp, K., Weinzierl, B., Esselborn, M., Hamburger, T., DöRNBRACK, A., et al. (2009). Saharan dust absorption and refractive index from aircraft-based observations during SAMUM 2006. *Tellus Series B: Chemical and Physical Meteorology*, *61*(1), 118–130. https://doi.org/10.1111/j.1600-0889.2008.00383.x

Piani, C., Haerter, J. O., & Coppola, E. (2010). Statistical bias correction for daily precipitation in regional climate models over Europe. *Theoretical and Applied Climatology*, *99*, 187–192. https://doi.org/10.1007/s00704-009-0134-9

Pitari, G., Di Genova, G., Coppari, E., De Luca, N., Di Carlo, P., Iarlori, M., & Rizi, V. (2015). Desert dust transported over Europe: Lidar observations and model evaluation of the radiative impact. *Journal of Geophysical Research – Atmospheres*, *120*, 2881–2898. https://doi.org/10.1002/2014JD022875

Pratt, K. A., & Prather, K. A. (2010). Aircraft measurements of vertical profiles of aerosol mixing states. *Journal of Geophysical Research*, *115*, D11305. https://doi.org/10.1029/2009JD013150

Prospero, J., Ginoux, P., Torres, O., Nicholson, S., & Gill, T. (2002). Enviromental characterization of global sources of atmospheric soil dust identified with the Nimbus 7 Total Ozone Mapping Spectrometer (TOMS) absorbing aerosol product. *Reviews of Geophysics*, *40*(1), 1002. https://doi.org/10.1029/2000RG000095

Pye, H. O. T., Chan, A. W. H., Barkley, M. P., & Seinfeld, J. H. (2010). Global modeling of organic aerosol: the importance of reactive nitrogen (NO_x and NO_3). *Atmospheric Chemistry and Physics*, *10*, 11261–11276. https://doi.org/10.5194/acp-10-11261-2010

Rastigejev, Y., Park, R., Brenner, M. P., & Jacob, D. J. (2010). Resolving intercontinental pollution plumes in globalmodels of atmospheric transport. *Journal of Geophysical Research*, *115*, D02302. https://doi.org/10.1029/2009JD012568

Ridley, D. A., Heald, C. L., & Ford, B. (2012). North African dust export and deposition: A satellite and model perspective. *Journal of Geophysical Research*, *117*. https://doi.org/10.1029/2011JD016794

Ridley, D. A., Heald, C. L., Pierce, J. R., & Evans, M. J. (2013). Towardresolution-independent dust emissions in global models: Impactson the seasonal and spatial distribution of dust. *Geophysical Research Letters*, *40*, 2873–2877. https://doi.org/10.1002/grl.50409

Rienecker, M. M., Suarez, M. J., Gelaro, R., Todling, R., Bacmeister, J., Liu, E., et al. (2011). MERRA: NASA's modern era retrospective analysis for research and applications, *J. Climate*, *24*(14), 3624–3648. https://doi.org/10.1175/JCLI-D-11-00015.1

Saleh, R., Marks, M., Heo, J., Adams, P. J., Donahue, N. M., & Robinson, A. L. (2015). Contribution of brown carbon and lensing to the direct radiative effect of carbonaceous aerosols from biomass and biofuel burning emissions. *Journal of Geophysical Research-Atmospheres*, *120*, 10285–10296.

Saleh, R., Robinson, E. S., Tkacik, D. S., Ahern, A. T., Liu, S., Aiken, A. C., et al. (2014). Brownness of organics in aerosols from biomass burning linked to their black carbon content. *Nature Geoscience*, *7*(9), 647–650. https://doi.org/10.1038/ngeo2220

Samset, B. H., Myhre, G., Schulz, M., Balkanski, Y., Bauer, S., Berntsen, T. K., et al. (2013). Black carbon vertical profiles strongly affect its radiative forcing uncertainty. *Atmospheric Chemistry and Physics*, *13*, 2423–2434. https://doi.org/10.5194/acp-13-2423-2013

Scanza, R. A., Mahowald, N., Ghan, S., Zender, C. S., Kok, J. F., Liu, X., et al. (2015). Modeling dust as component minerals in the Community Atmosphere Model: development of framework and impact on radiative forcing. *Atmospheric Chemistry and Physics*, *15*, 537–561. https://doi.org/10.5194/acp-15-537-2015

Scarnato, B. V., Vahidinia, S., Richard, D. T., & Kirchstetter, T. W. (2013). Effects of internal mixing and aggregate morphology on optical properties of black carbon using a discrete dipole approximation model. *Atmospheric Chemistry and Physics*, *13*, 5089–5101. https://doi.org/10.5194/acp-13-5089-2013

Schulz, M., Textor, C., Kinne, S., Balkanski, Y., Bauer, S., Berntsen, T., et al. (2006). Radiative forcing by aerosols as derived from the AeroCom present-day and pre-industrial simulations. *Atmospheric Chemistry and Physics*, *6*(12), 5225–5246. https://doi.org/10.5194/acp-6-5225-2006

Shell, K. M., & Somerville, R. C. J. (2007). Sensitivity of climate forcing and response to dust optical properties in an idealized model. *Journal of Geophysical Research*, *112*, D03206. https://doi.org/10.1029/2006JD007198

Sinyuk, A., Torres, O., & Dubovik, O. (2003). Combined use of satellite and surface observations to infer the imaginary part of refractive index of Saharan dust. *Geophysical Research Letters*, *30*(2), 1081. https://doi.org/10.1029/2002GL016189

Sokolik, I. N., & Toon, O. B. (1999). Incorporation of mineralogical composition into models of the radiative properties of mineral aerosol from UV to IR wavelengths. *Journal of Geophysical Research*, *104*(D8), 9423–9444.

Souri, A. H., Choi, Y., Pan, S., Curci, G., Nowlan, C. R., Janz, S. J., et al. (2018). First top-down estimates of anthropogenic NOx emissions using high-resolution airborne remote sensing observations. *Journal of Geophysical Research*. https://doi.org/10.1002/2017JD028009

Streets, D. G., Zhang, Q., Wang, L., He, K., Hao, J., Wu, Y., et al. (2006). Revisiting China's CO emissions after the Transport and Chemical Evolution over the Pacific (TRACE-P) mission: Synthesis of inventories, atmospheric modeling, and observations. *Journal of Geophysical Research*, *111*(D14), D14306. https://doi.org/10.1029/2006JD007118

Tegen, I., Werner, M., Harrison, S. P., & Kohfeld, F. E. (2004). Relative importance of climate and land use in determinating present and future global soil dust emissions. *Geophysical Research Letters*, *31*, L05105. https://doi.org/10.1029/2003GL019216

Toon, O. B., & Ackerman, T. P. (1981). Algorithms for the calculation of scattering by stratified spheres. *Applied Optics*, *20*(20), 3657–3660. https://doi.org/10.1364/AO.20.003657

Updyke, K. M., Nguyen, T. B., & Nizkorodov, S. A. (2012). Formation of brown carbon via reactions of ammonia with secondary organic aerosols from biogenic and anthropogenic precursors. *Atmospheric Environment*, *63*, 22–31. https://doi.org/10.1016/j.atmosenv.2012.09.012

Van der Werf, G. R., Randerson, J. T., Giglio, L., Collatz, G. J., Mu, M., Kasibhatla, P. S., et al. (2010). Global fire emissions and the contribution of deforestation, savanna, forest, agricultural, and peat fires (1997–2009). *Atmospheric Chemistry and Physics*, *10*, 11707–11735. https://doi.org/10.5194/acp-10-11707-2010

Vignati, E., Karl, M., Krol, M., Wilson, J., Stier, P., & Cavalli, F. (2010). Sources of uncertainties in modelling black carbon at the global scale. *Atmospheric Chemistry and Physics*, *10*, 2595–2611. https://doi.org/10.5194/acp-10-2595-2010

Wagner, R., Ajtai, T., Kandler, K., Lieke, K., Linke, C., Müller, T., et al. (2012). Complex refractive indices of Saharan dust samples at visible and near UV wavelengths: a laboratory study. *Atmospheric Chemistry and Physics*, *12*, 2491–2512. https://doi.org/10.5194/acp-12-2491-2012

Wang, X., Heald, C. L., Liu, J., Weber, R. J., Campuzano-Jost, P., Jimenez, J. L., et al. (2018). Exploring the observational constraints on the simulation of brown carbon. *Atmospheric Chemistry and Physics*, *18*, 635–653. https://doi.org/10.5194/acp-18-635-2018

Wang, X., Heald, C. L., Ridley, D. A., Schwarz, J. P., Spackman, J. R., Perring, A. E., et al. (2014). Exploiting simultaneous observational constraints on mass and absorption to estimate the global direct radiative forcing of black carbon and brown carbon. *Atmospheric Chemistry and Physics*, *14*, 10989–11010. https://doi.org/10.5194/acp-14-10989-2014

Wang, X., Heald, C. L., Sedlacek, A. J., de Sá, S. S., Martin, S. T., Alexander, M. L., et al. (2016). Deriving brown carbon from multiwavelength absorption measurements: method and application to AERONET and Aethalometer observations. *Atmospheric Chemistry and Physics*, *16*, 12733–12752. https://doi.org/10.5194/acp-16-12733-2016

Wang, Y. Y., Liu, F. S., He, C. L., Bi, L., Cheng, T. H., Wang, Z. L., et al. (2017). Fractal dimensions and mixing structures of soot particles during atmospheric processing. *Environmental Science & Technology Letters*, *4*, 487–493.

Yan, C., Zheng, M., Bosch, C., Andersson, A., Desyaterik, Y., Sullivan, A. P., et al. (2017). Important fossil source contribution to brown carbon in Beijing during winter. *Scientific Reports*, *7*, 43182. https://doi.org/10.1038/srep43182

Zarzycki, C. M., & Bond, T. C. (2010). How much can the vertical distribution of black carbon affect its global direct radiative forcing? *Geophysical Research Letters*, *37*, L20807. https://doi.org/10.1029/2010GL044555

Zender, C. S., Bian, H., & Newman, D. (2003). Mineral Dust Entrainment and Deposition (DEAD) model: Description and 1990s dust climatology. *Journal of Geophysical Research*, *108*. https://doi.org/10.1029/2002JD002775

Zhang, L., Kok, J., Henze, D. K., Li, Q. B., & Zhao, C. (2013). Improving simulations of fine dust surface concentrations over the Western United States by optimizing the particle size distribution. *Geophysical Research Letters*, *40*, 3270–3275. https://doi.org/10.1002/grl.50591

Zhang, L. M., Gong, S. L., Padro, J., & Barrie, L. (2001). A sizesegregated particle dry deposition scheme for an atmospheric aerosol module. *Atmospheric Environment*, *35*, 549–560.

Zhang, X. L., Lin, Y. H., Surratt, J. D., & Weber, R. J. (2013). Sources, composition and absorption Ångström exponent of light absorbing organic components in aerosol extracts from the Los Angeles Basin. *Environmental Science & Technology*, *47*(8), 3685–3693. https://doi.org/10.1021/es305047b

Zhang, X. L., Mao, M., Yin, Y., & Wang, B. (2017). Absorption enhancement of aged black carbon aerosols affected by their microphysics: A numerical investigation. *Journal of the Optical Society of America*, *202*, 90–97.

Zhang, Y., Forrister, H., Liu, J., Dibb, J., Anderson, B., Schwarz, J. P., et al. (2017). Top-of-atmosphere radiative forcing affected by brown carbon in the upper troposphere. *Nature Geoscience*, *10*(7), 486–489. https://doi.org/10.1038/ngeo2960